The Pennsylvania State University

Schreyer Honors College

Department of Materials Science and Engineering

SYNTHESIS AND CHARACTERIZATION OF NOVEL 2D HETEROSTRUCTURE MATERIALS

Brian D. Markman
December 2015

A thesis submitted in partial fulfillment of the requirements for a baccalaureate degree in Materials Science and Engineering with honors in Materials Science and Engineering

Reviewed and approved* by the following:

Joshua Robinson
Assistant Professor of Materials Science and Engineering
Thesis Supervisor

Allen Kimel
Assistant Professor of Materials Science and Engineering
Honors Adviser

*Signatures are on file in the Schreyer Honors College.

Abstract

Hexagonal boron nitride (h-BN) and transition metal dichalcogenides (TMD) have received increased attention in recent years due to graphene's lack of bandgap. Hexagonal boron nitride exhibits some key advantages over 3D dielectrics such as its atomically smooth surface and lack of dangling bonds. Monolayer transition metal dichalcogenides exhibit interesting properties as compared to their multilayer counterparts. Most notable is the indirect-direct bandgap transition that TMDs undergo with layer thinning.

This thesis presents the CVD growth of h-BN on Cu foil and the ARPES investigation of h-BN grown in UHV on Pt(110). Growths in UHV demonstrate the possibility of low temperature (630°C) ordered growth. Additionally, intercalation of Au to reach a quasi-free standing state was demonstrated and direct growth of WS_2 on h-BN grown on Au and Ni(111) was also demonstrated.

Direct growth of WS_2 in UHV on various substrates (metallic and insulating) was also demonstrated. Low temperature growths (120°C) resulted in a disordered metallic phase while annealing to 400°C resulted in an irreversible phase transformation to the thermodynamically, semiconducting phase. The direct growth of the metallic phase occurred preferentially on quasi-free standing h-BN as compared to Au due to reduced coupling between layers and reduced adherence of residual S to the surface.

Table of Contents

List of Figures

List of Tables

List of Equations

Acknowledgements

I would like to thank my family – my mom, dad, and sister – for being supportive of me all the way through my college and research careers. They not only supported but also guided me along the way. I'd also like to thank the rest of my family – aunts, uncles, cousins, and grandmothers – for supporting me.

Additionally I would like to graciously thank my research advisors along the way; there have been quite a few, but specifically I would thank to thank Dr. Robinson for helping me through the process of writing my thesis as well as sending me abroad to conduct research in Italy. Thank you for your flexibility and support along the way. Also, I would like to thank Dr. Granozzi for hosting me while abroad in Italy and exposing me to a different approach to the same problem.

Furthermore, I would like to thank Dr. Giebink for giving me my first taste or research as well as Dr. Agnew and Dr. Rodwell for hosting over the past two summers. Finally, I would like to thank Abe, Mattia, Stefano, Hua, Rob, Prateek, Chris, and all of the other grad students/post docs that I have directly worked with over the past four years. Thank you all for your advice, guidance, encouragement, patience, and support.

I would like to thank Abe specifically for helping me with all things h-BN. I would also like to thank Mattia for teaching me everything I need to know UHV, WS_2, and Italy. I would like to thank all of the graduate students and undergraduate students in Dr. Robinson's group as well as the graduate students in Dr. Granozzi's group. Additional thanks to members of the materials research center at Penn State for providing a clean, safe environment to work in and for providing support with technical and mechanical problems. And finally, I would like to thank all of my friends, classmates, and lab-mates.

1. Introduction / Literature Review

1.1 Introduction to 2D Materials

Two-dimensional (2D) materials have generated a large amount of attention since the (re)discovery of single layer graphene in 2004 by Novoselov and Geim and the subsequent demonstration of the many unusual properties that can be found in monolayer and few layer material systems,[1–3] including thermal conduction, electrical resistivity, and various mechanical properties have attracted interest in these materials from many fields.[1] Specifically hexagonal boron nitride (h-BN) and transition metal dichalcogenides (TMDs) are of interest because of their potential applications in sensors, transistors, thermal barriers, and, in some cases, high temperature superconductors.[1,4,5] Despite the demonstration of exfoliation, both mechanical and chemical, by Frindt *et al*. in 1966, research to adequately characterize these materials did not exist until after 2004.[1,6] With the demonstration of graphene's unique properties in 2004, research in both TMDs and h-BN surged as well.[1]

As a result of this renewed interest, 2D materials research has matured very quickly and has seen vast improvements in fabrication, characterization, and implementation over the past 10 years.[1] These improvements have led to fabrication methods including solution based, solvothermal, UHV epitaxial vapor, chemical vapor, and many others, thus demonstrating the versatility and adaptability of these materials.[1]

This thesis will focus on the chemical vapor deposition and Raman spectroscopy characterization of h-BN grown with ammonia borane precursor in low vacuum. Additionally, it will feature a detailed study the physical vapor deposition (PVD) and photoelectron spectroscopy (PES) characterization of tungsten disulfide (WS_2) material systems in ultra high vacuum

(UHV). Finally, a brief further section will include the ARPES characterization of tungsten diselenide (WSe_2).

1.2 Fundamental Properties, Fabrication, and Characterization of Hexagonal Boron Nitride

Boron nitride is a III-V compound which is a class of solid compounds containing one group III element and one group V element bonded together. Many such structures adopt the Sphaelerite or Wurtzite structures at room temperature; Boron nitride exists in four different structures: hexagonal, cubic, wurtzite, and amorphous.[7,8] Hexagonal boron nitride is of particular interest and one of the focuses of this thesis because it is an insulating (E_g ~ 5.97 eV), isomorph of graphene.[7,10] The most widely accepted band diagram of h-BN is shown below in **Figure 1.2.1**.[10] As a result, BN has already attracted research attention and has been fabricated via metalorganic vapor phase epitaxy,[7,11] various forms of chemical vapor deposition,[12–16] and atomic layer deposition,[17] among other deposition methods.

Not only is h-BN structurally well suited for electronic applications with graphene, it is also chemically inert to many acids, thus making it an attractive material for device fabrication, and is thermally stable, while also being thermally conductive (in-plane thermal conductivity of 390 W/mK).[18,19]

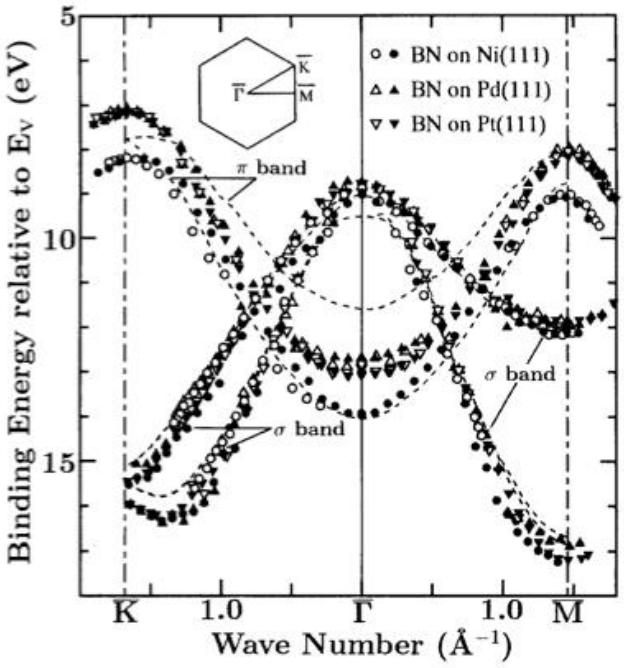

Figure 1.2.1 Most widely accepted E-k diagram of h-BN as measured by Nagashima *et al* where only the Γ-K and Γ-M direction are of interest.[10]

Similar to graphene and other 2D materials, h-BN exhibits anisotropic properties;[7] specifically of interest are the coefficient of thermal expansion (CTE) which is negative in plane and positive out of plane (in the c direction).[19] This is a consequence of the weak van der Waal's bonds that bind the layers together and has made h-BN an attractive material to be used as a dry thermal lubricant.[7]

The most widely accepted phase diagram of boron nitride is illustrated below in **Figure 1.2.2**.[20] It is worth noting that cubic boron nitride (c-BN) is the most thermodynamically stable phase below ~1600K; however, h-BN is frequently realized at temperatures ranging as low as 1073 K on transition metal substrates – in fact in this thesis hBN was grown on Ni at 973 K.[7] It has been demonstrated in Kern *et al.* that the transition temperature of c-BN/h-BN systems are greatly affected by a small change in the Gibb's Free Energy of the system where a ±10 meV/atom difference places a stable range for h-BN between 1200-1800 K.[21] The lower end of this range falls within typical growth temperatures for h-BN.[7]

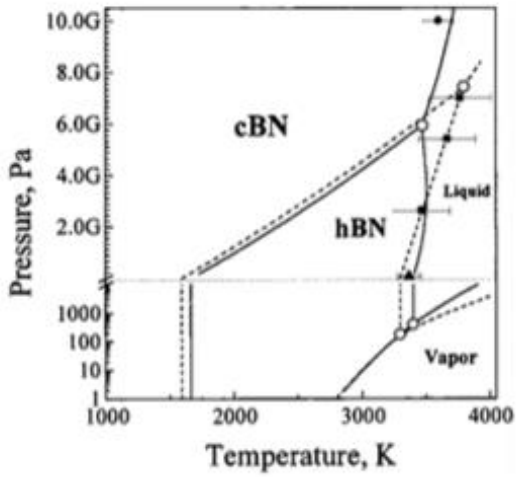

Figure 1.2.2 The most widely pressure-temperature phase diagram of BN compounds as published by Solozhenko and Turkevich.[20]

Because of the large effect caused by minor differences, it can be difficult to experimentally control what phase of boron nitride is grown.[7] However, Raman spectroscopy can quickly determine between phases. Cubic boron nitride contains two modes that are Raman active – both optical modes – a transverse and a longitudinal.[21] The transverse optical (TO) mode is located at ~1055 cm^{-1} while the longitudinal optical (LO) mode is located at ~1304 cm^{-1}. Hexagonal boron nitride only contains a single Raman active mode, a degenerate TO/LO that causes out of phase oscillations of the B and N atoms; it is located at 1364 cm^{-1}. Consequently, the two phases are easily distinguishable.[21]

In summary, hexagonal boron nitride is an attractive material for integration into 2D microelectronics devices and systems including graphene due to its high thermal conductivity, chemical stability, and electrical insulation. Although c-BN is thermodynamically more stable, h-BN is easily attainable due to the variation in the Gibb's Free Energy in systems containing transition metal substrates. Finally, h-BN can be readily determined by and distinguished from other BN phases by Raman spectroscopy.

1.3 Fundamental Properties, Fabrication, and Characterization of Tungsten Disulfide

Tungsten disulfide (WS_2) is a transition metal dichalcogenide (TMD). TMDs conform to the general formula of MX_2 where M is a transition metal and X is a chalcogen (S, Se, Te).[22,23,24,25] Because of this, TMDs exhibit excellent versatility in electrical, chemical, and mechanical properties.[22,25–29] Changes to the metal and the chalcogen can both have profound effects on the behavior of the material within a system or environment.[22,30,31]

For example, some TMDs are semiconducting (MoS_2), semimetallic (WTe_2), and even metallic (NbS_2).[26] Many monolayer TMDs also exhibit interesting and different properties when compared to their bulk materials.[26,27,3130,32] For example, bulk MoS_2 is an indirect bandgap semiconductor while monolayer MoS_2 is a direct bandgap semiconductor.[22,30,32]This change is a consequence of the lack of interlayer coupling and inversion symmetry in monolayer material systems;[23,27] specifically, the lack of interlayer coupling can dramatically alter the electronic band structure of the material while the lack of inversion symmetry allows for interesting optical activity.[23,27]

TMDs generally exist in a few different crystallographic phases though the most common include trigonal prismatic and octahedral phases.[22,33] In the octahedral phase, chalcogen atoms are directly bonded to the transition metal and are located rotated 60° as compared to their symmetrically related counterparts; the trigonal prismatic phase contains a 60° rotation of the top chalcogen layer with respect to the bottom chalcogen layer which superimposes the top chalcogen layer over the bottom.[22] While atoms in each layer are strongly covalently bonded, layers are loosely bound by van der Waal's forces;[22,26,27] this makes mechanical sheering and exfoliation of layers relatively easy when compared to a 3D crystal.[22,26]

It has been demonstrated that monolayer, semiconducting films of TMDs, such as WS_2 and MoS_2, can be mechanically exfoliated[27,34] or fabricated via CVD, pulsed laser deposition (PLD)[35], and PVD and are stable under ambient temperature and pressure. Additionally, layered TMDs can be used for catalysis, energy storage, and electronics.[22,26–31]

Though graphene is the most famous 2D material and has been extensively studied, it is a zero bandgap semiconductor and can only realize a small bandgap upon doping or substrate coupling which adversely affects other electronic properties such as mobility.[1,22,25,26] As a result, interest in TMDs in recent years has been growing as a possible alternative to graphene for applications including flexible electronics and optoelectronics.[22,24] Because most monolayer TMDs possess a direct bandgap of <2.0 eV, they are of great interest to the electronics industry.[22,25] Monolayer MoS_2 has attracted much attention because, of the TMDs, it contains a bandgap of 1.86 eV and is stable at room temperature.[25]

While other TMDs are also attractive due to the existence of smaller bandgaps and reduced carrier effective masses. Additionally, metallic and wider bandgap TMDs are also desirable for various applications. Despite many previous studies to characterize MoS_2, work on WS_2 to date is incomplete. Consequently, the interest of this thesis is the fabrication and characterization of WS_2 on various substrates. Like other TMDs, WS_2 exists in two primary forms: a metastable, metallic phase (1T) and a thermodynamically favored, semiconducting phase (2H) where the 1T phase is octahedral while the 2H phase is trigonal prismatic. Because of the metastable nature of the 1T phase, it is difficult to realize stable isolation of this phase. Also, it is possible to irreversibly convert the 1T phase to the thermodynamically favored 2H by annealing at temperatures >300°C.

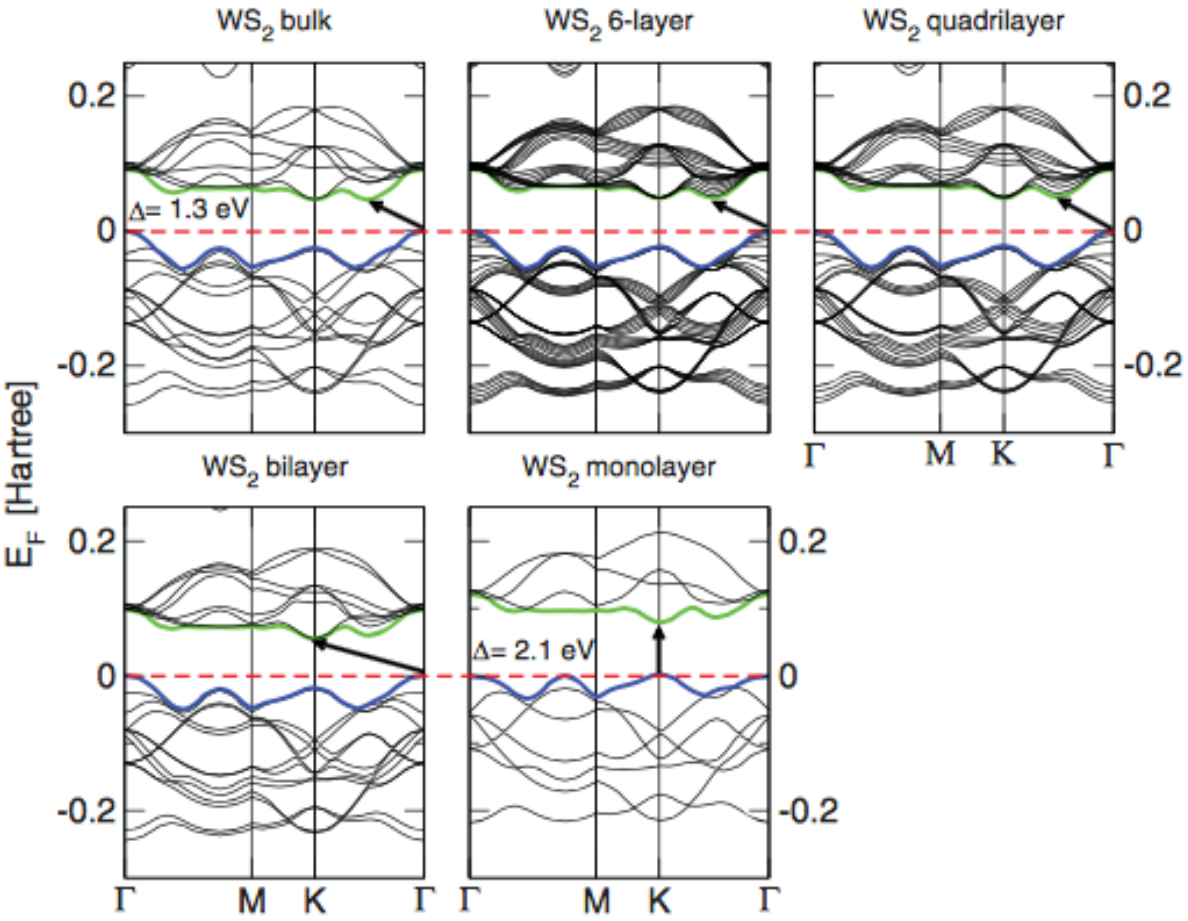

Figure 1.3.1 Calculated band structure of WS_2 as a function of thickness (ranging from bulk to monolayer) as published by Kuc *et al.*[36]

Monolayer 2H-WS_2 is attractive because it is more resistant to oxidation than monolayer MoS_2 at temperatures up to 100°C and has a direct bandgap of 2.1 eV which is a function of the film thickness[36]: a diagram demonstrating the evolution of the WS_2 band diagram as a function of thickness is shown above in **Figure 1.3.1**. Additionally, WS_2 can be readily grown on transition metal surfaces and electronically decoupled from the surface using an insulator such as h-BN.[37] Adjusting the thickness of the insulating layer can control the extent of decoupling;[37] the same technique can be used to control the interlayer coupling of TMD heterostructures thus allowing for a wide range of TMD optoelectronics to be realized.[37]

Metallic WS_2 is also catalytically active and is used in hydrotreating, hydrocracking, and hydrogen evolution reactions.[28,29,38,39] In particular, 1T-WS_2 has demonstrated performances approaching that of commercial platinum catalysts; optimization of direct 1T-WS_2 growths could have wide reaching implications for alternative energy technologies.

Because of the catalytic activity and need for very low contact resistances for the microelectronics industry,[25] direct growth of 1T-WS_2 is desirable. Literature reports alkali intercalation of 2H-WS_2,[40] colloidal synthesis,[29] and stabilization by donor doping of 2H nanoribbons[41] in an attempt to realize stable 1T-WS_2. However, alkali intercalation introduces strain and disorder, colloidal synthesis yields low crystallinity, multilayered sheets, and donor doping of nanoribbons is dependent on the existence of a 2H inner nanoribbon.[29,40,41] Thus direct deposition of high quality monolayer 1T-WS_2 has yet to be achieved.

This thesis will discuss the deposition of WS_2 on Ni(111), Au/Ni(111), h-BN/Ni(111), and h-BN/Au/Ni(111) systems at 120°C and subsequent annealing to 400°C. Crystal structure was determined via LEED, the core electronic structure was determined via XPS, and the valence band structure was determined via UPS. No LEED pattern was discernable for a 1T-like phase though the metallic nature was observed via UPS. Additionally, 1T-like characteristics were observed via XPS. We hypothesize that our observed phase is either amorphous or lacks azimuthal orientation and consequently does not have a defined LEED pattern. For simplicity and for agreement with previous literature, from this point forward this 1T-like phase will be referred to only as “1T” phase.

1.4 Introduction to Chemical Vapor Deposition

Chemical vapor deposition is a technique to deposit a thin layer of solid material on another solid substrate.[42–44] This deposition occurs as a result of chemical reactions that occur in

the vapor phase and cause condensation on a substrate.[42–44] Often times a catalytic transition metal surface can be used as the substrate material.[45] CVD strongly depends on the transport and kinetics of gaseous precursors in order to generate the desired reaction.[46] Thus the selection of precursor gases, carrier gases, pressure, and temperatures can all have profound effects on the outcome of a particular setup.[42,46]

Most basically, the parameters that determine the deposition rate and subsequent film quality are the mass transfer into and out of the system – governed mainly by pressure – and the reaction rate – governed primarily by temperature and precursor.[46] Because samples are generally loaded with their surface normal vector perpendicular to the flowing gas, it is important to consider how the gas (the reactant) reaches the surface.[46] Because a boundary layer forms over the surface of the solid, it is important to consider the diffusivity of the precursor gas and the parameters of the boundary layer in order to determine your mass transfer at the surface of your substrate.[46] Because with decreased pressure, you have significantly increased diffusivity, it is clear that the mass transfer to a surface under low pressure is much greater than in a high-pressure system.[46]

In low-pressure systems, the reaction rate of species at the surface governs the coating of the surface.[47] This is because the mean-free-path of the gas is larger than the thickness of the boundary; consequently this means that the boundary layer is negligible.[47] This suggests that because the surface is not saturated with gas at all times (i.e. a negligible stagnant layer) that the rate at which the reaction will occur governs the deposition rate.[47] Film quality is then governed in part by these reactions. Because CVD depends on the decomposition of carrier gases, it is important to consider where and how these reactions occur. If reactions occur in the gas phase

then particles of the desired material will generally form and fall to the surface generated a polycrystalline, 3D film of low density.[47]

Thus it is more desirable to have deposition that occurs due to reaction at the substrate surface.[47] However, in this regime the prior mentioned mechanism is still important to consider as it can contribute to defect formation and reduce film quality.[47] In order to achieve conformal coverage and higher quality films it can be important to include inert carrier gases to control the flux of reactive species at the surface as well as pressure and gas velocity.[47] After a reactant reaches the surface, sticking coefficient and surface mobility are of importance.[47] Not only does the reactive species have to stick to the surface, but it must migrate on the surface until it collides and reacts with another stuck species to generate a film.[47] Atoms or molecules stuck to the surface can also return to the gas phase before reacting;[47] this must be considered when designing a process. Because CVD is often carried out at elevated temperatures, the tendency for material adsorbed to the surface to return to the gas phase can be quite high.[47]

It is clear that to obtain uniform coverage of a sample, it is very important to control the temperature, pressure, precursor gas, carrier gases, and reactor geometry.[43,44,47] Selection of each parameter can affect coverage, chemistry, density, and other properties.[42–44,46] Because CVD is often performed at elevated temperatures, ~1000°C, various CVD techniques are often named for the precursor or pressure used; for example, metal organic CVD (MOCVD) uses metal organic precursors to enable lower temperature growth while low pressure CVD (LPCVD) uses a low pressure configuration, $\sim 10^{-1} - 10^{-2}$ Torr, to increase the deposition rate and decrease defect density of the deposited film.

Advantages of CVD include conformal coverage, a wide selection of precursors, relatively low deposition temperatures (refractories can be deposited via reactions much lower

than their melting points), control over crystal structure, and ability to be implemented without complex and expensive UHV systems.[42,44] Despite the many advantages, disadvantages of CVD include potentially toxic or harmful precursors, complex, sometimes uncontrollable, reactions with multiple products, as well as non-self-limiting reactions, and the inability to deposit stoichiometrically controlled multi-component materials.[44] As aforementioned, many different subcategories of CVD exist, many addressing one, or multiple, of these, and other, problems in an attempt to optimize the process for a given application: for example, atomic layer deposition (ALD) is a self-limiting version of CVD.[44] A schematic of the CVD furnace used in this thesis can be found in the experimental section in Figure 2.1.1.

Because of the versatility and industrial scalability, CVD became a key technique used by the microelectronics industry[48] and has since been adopted to deposit many 2D materials such as graphene, hBN, TMDs, and various other 2D materials.[1,25,49]

Specifically, LPCVD is of great interest for 2D materials because of the reduced defect density – a common problem of 2D materials – improved coverage, and improved film quality when compared to atmospheric pressure CVD.[50] Interestingly, in some cases, reduced pressure generates higher nucleation and increased defect density as described by Eichfield *et al* for the growth of WSe_2 on various substrates.[51] In this case, MOCVD growth observed a 3x increase in domain size as deposition pressure was increased.[51] Domain size was found to be further dependent on temperature;[51] this suggests a low sticking coefficient and low surface mobility. This can be conceptualized by considering that increased pressure increased domain size suggesting that with increased pressure, more atoms can adhere to the surface at any given time. Increasing the temperature provides these atoms with surface mobility further increasing domain size as well as further promoting reduction of the organic ligands of the precursor gas. Thus,

while decreased pressure often leads to decreased defect density, it is important to consider each system individually.

These traits are pertinent to obtain the improved electronic properties necessary to make 2D materials competitive with modern silicon electronics. Additionally, manufacturing with LPCVD reduces cost due to higher possible output as uniform, conformal growth remains possible even with higher packing density of die in a growth chamber.[46] This is a direct result of improved mass transport through narrow gaps under low pressure.[46]

Finally, because so many variations of CVD exist and because multiple variations are effective at growing a wide range of 2D materials, CVD is an attractive fabrication technique not only to experiment with 2D materials but also to manufacture them.

1.5 Introduction to Physical Vapor Deposition

Physical vapor deposition is a method of depositing thin films in which a solid precursor is transformed into a gaseous state by some form of thermal or impact evaporation.[52] Single atoms, molecules, and small molecular clusters can be ejected from the source and will then deposit on both the walls of the preparation chamber as well as the sample.[52] When performed in ultra high vacuum (UHV), the mean free path of the particles can be larger than that of the vacuum chamber and can lead to uneven coating of the substrate depending on the location and particle beam focus.[52]

Because the particles ejected from the source generally contain high kinetic energy, many properties of a thin film can be affected including density and electrical conductivity.[47] As a result, implementation of various different PVD techniques can enable improved control over many material properties. One of the major advantages is that metastable phases, phases integral to performance in certain applications, can be directly deposited with a stable lifetime.[52]

Additionally, some PVD techniques allow for conformal coating over high aspect ratio structures.[53] Variations of PVD, including ionized PVD (IPVD) also allow for the directed growth of films under specifically designed electric fields.[53] Like CVD, many variations of PVD exist and address particular problems necessary for each application.[52,53] The most common way to tailor a PVD technique is to alter the vaporization process: techniques include: thermal evaporation, electron beam (e-beam) evaporation, pulsed laser evaporation, sputter, and plasma decomposition.[52,53]

Each technique produces different ejected molecule sizes, energies, and types.[52] Some techniques, such as plasma decomposition, produce a high quantity of ions while other techniques, such as thermal evaporation, do not.[52] Additionally, some methods yield single atom or molecule particles while others produce atom/ion clusters.[52]

In this thesis, electron beam (e-beam) evaporation and thermal evaporation techniques were used to deposit tungsten and gold. In electron beam evaporation, a tungsten wire is resistively heated until thermionic emission occurs.[47] Ejected electrons are then accelerated in an electric field where the impact the sample ejecting particles from the surface.[47] These particles then travel until they deposit on the sample surface or chamber walls.[47] Because these particles often contain high kinetic energy, they can rearrange on the surface to an extent.[47] The mean-free-path of the ejected particles is larger than the chamber size (many times greater in UHV) and thus e-beam evaporation is a line of sight deposition process, meaning that non-conformal films are produced.[47] Thus, in this thesis, the sample was placed so that the spot size of the deposition was larger than the sample in order to promote conformal coverage.

Thermal evaporation occurs when a wire or boat of the desired material to deposit is heated until the material is ejected from the surface.[47] This can happen by two different

mechanisms: evaporation or sublimation.[47] Evaporation occurs when particles are ejected from a molten material while sublimation occurs when particles are ejected from a solid sample directly into the gas phase.[47] Because both mechanisms require the sample to be heated to T > 1200°C for many metals (above their melting temperature);[47] because of the very high T_{melt} of refractories, thermal evaporation is not a realistic process and e-beam evaporation is often used. The mechanism with which particles are ejected is material, temperature, and pressure dependent and will not be discussed in detail in this thesis. While thermally evaporated materials often have more conformal coverage than e-beam evaporated materials due to reduced mean-free-path of ejected particles, in a UHV system this cannot be assumed.

A schematic of the UHV chamber with PVD capability is demonstrated in the experimental section in Figure 2.2.1. This thesis utilized e-beam evaporation and thermal evaporation methods to deposit Au and W layers where the production of ions is assumed to be low and the gas composition is assumed to be a mixture of atoms and atomic clusters. Samples were placed directly in the particle beam line where the beam focus was larger than the target crystal thus insuring conformal growth. Samples were then tested via XPS and their integrated intensities, measured in multiple positions, were considered in order to determine that homogeneous coverage of the surface had been achieved.

1.6 Fundamentals of Angular Resolved Photoelectron Spectroscopy

The photoelectric effect, the principle governing photoelectron spectroscopy (PES), was first observed by Hertz and later made famous by Albert Einstein.[54–56] The photoelectric effect says that an electron in a solid can absorb an energetic photon; with the absorbed kinetic energy, the electron can then escape from the solid.[56] By measuring the momentum of the ejected photoelectron and knowing the energy of the incident photon, it is possible to determine

important information regarding the electronic structure of the solid.[57–59] As a result, the ejected electron will have kinetic energy equal to the incident photon energy minus the work function of the solid as demonstrated in the equation below:

$$E_{kin} = h\upsilon - \phi$$

Equation 1.6.1. Einstein's equation describing the photoelectric effect

where E_{kin} is the kinetic energy of the ejected electron, h is Planck's constant, ν is frequency of the photon, and ϕ is the work function of the material.[54,56] This effect can be utilized with a range of incident photon energies.[54] For example, when high-energy incident photons are used – such as x-rays – it is possible to eject core level electrons while low energy incident photons – such as ultraviolet rays – can eject valance band electrons. Thus by using different photon energies, it is possible to obtain valuable information about the composition (core level electrons) and bonding (valence electrons) of a system by using PES.

This technique is even more powerful when one considers the introduction of angular resolution; a diagram illustrating the variables to be considered when adding this complexity can be found below in **Figure 1.6.1**. Because the momentum of an electron can be considered by its individual components:

$$K_{tot} = \overrightarrow{K_{\perp}} + \overrightarrow{K_{\parallel}}$$

Equation 1.6.2 The total kinetic energy (K_{tot}) expressed as the components of kinetic energy perpendicular and parallel to the surface of the sample

where:

$$\overrightarrow{K_{\parallel}} = \overrightarrow{K_x} + \overrightarrow{K_y}$$

Equation 1.6.3 Kinetic energy parallel to the surface of the sample can be rewritten in Cartesian coordinates where the surface of the sample is assumed to be an infinite xy-plane

and:

$$\overrightarrow{K_{\perp}} = \overrightarrow{K_z}$$

Equation 1.6.4 Kinetic energy perpendicular to the surface of the sample; component of most interest because the kinetic energy is reduced as the electron overcomes the metal work function

Because during the process of photoemission, some of the components of an electrons momentum are preserved while others are not, it possible to determine information of epitaxial samples in specific crystallographic directions;[54] specifically, electron momentum parallel to the surface of the solid is preserved while momentum perpendicular is not preserved.[54] This is because momentum perpendicular to the surface is lost overcoming the work function of the solid, an inherent potential difference between the environment of the solid and vacuum,[54,56] while this barrier does not exist parallel to the surface.[54]

Additional subtleties arise when the ejected electron is considered as a wave and Snell's law is taken into consideration.[57] As a result, the electron propagating inside the solid and the electron propagating outside the solid have vastly different energies and slightly different angles.[54,57] It is important to consider both of these variables in order to determine the electron's origin.

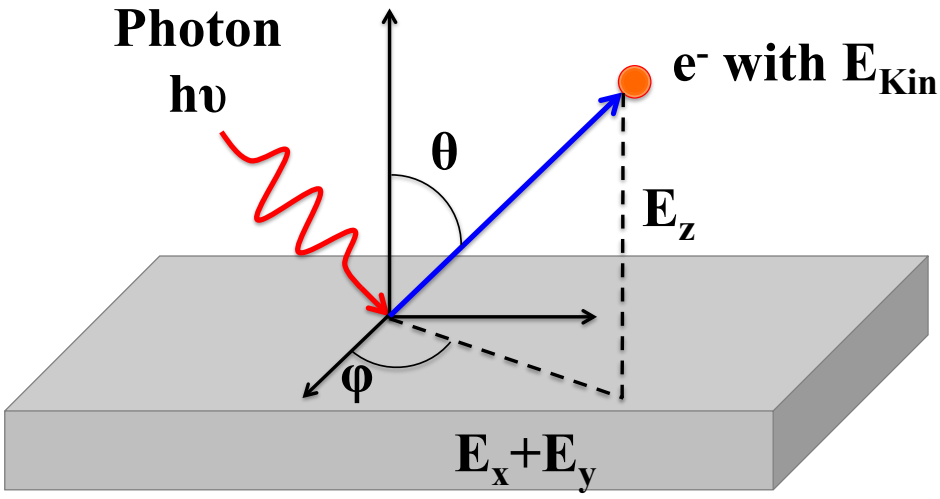

Figure 1.6.1 Diagram depicting the angular and energetic components of an incoming photon and outgoing electron to be considered during ARPES where the energy in-plane is conserved and the energy out of plane is not conserved.

Consequently, examining different angles enables you to ‘filter’ electron momenta and, thus, scan along crystallographic directions. Though, because of the two degrees of freedom, scanning all energies and all angles is not experimentally feasible with a 1D detector; however, with the introduction of 2D and 3D detectors it became possible to filter through multiple energies and angles simultaneously creating an efficient and realistic method to experimentally observe band dispersions of many materials.[57,59]

One drawback of ARPES is the necessity for a single crystalline or epitaxial sample. Because some 2D materials can be grown epitaxially on a wide variety of substrates and exhibit electronic properties that differ from their equivalent bulk materials and due to their inherent lack of 3D symmetry, 2D materials can be easily and quickly measured and analyzed via ARPES. As a result, 2D materials grown on various substrates are an exciting field to be explored via ARPES. Results will lead to a better understanding of substrate coupling on the electronic band structure of this class of materials which will ultimately lead to improved material implementation and device design. It is worth noting that there are many new 2D materials that have yet to have their electronic structures mapped; thus ARPES studies of evolving 2D materials and 2D heterostructures is an exciting field.

2 Equipment and Experimental Procedures

2.1 Chemical Vapor Deposition of Hexagonal Boron Nitride

All CVD h-BN samples were grown on polycrystalline Cu foil at 1000-1050°C. Copper foils were cut to 5 cm x 5 cm and smoothed by placing between two chemwipes and mechanically rubbing using the smooth, backside of a Sharpie. In some cases, Cu foil was electro-polished using a Cu|H_3PO_4|Pt electrochemical cell at 7.88 V for 60 seconds. These substrates were then loaded into the CVD reactor were they were heated to 1050°C for 2 hours

with flowing Ar and H in order to remove any oxide layer. The annealing time allowed for grain growth and surface defect reduction thus decreasing the nucleation sites during h-BN growth.

Ammonia borane (NH_3BH_3) was used as the precursor and was heated to 60°C and then pumped to alleviate H generated during the first and second hydrogen evolutions. The sublimation chamber was then further heated to 100°C for 10 minutes and pumped to evaporate any water; finally it was heated to 130°C and allowed to sit for 5-15 minutes in order to allow enough pressure to accumulate to sustain the designed deposition.

Samples were then exposed to ammonia borane with an Ar carrier gas for 2-10 minutes at flow rates ranging from 2.5-10 sccm and pressures of 350-700 mTorr. The flow rate of ammonia borane was controlled using a MKS Instruments Type 1150 mass flow rate controller while the flow rates of Ar and H_2 were controlled using two identical MKS Instruments Type 1179 mass flow rate controllers. An illustration of the CVD system used for h-BN deposition is shown below in Figure 2.1.1.

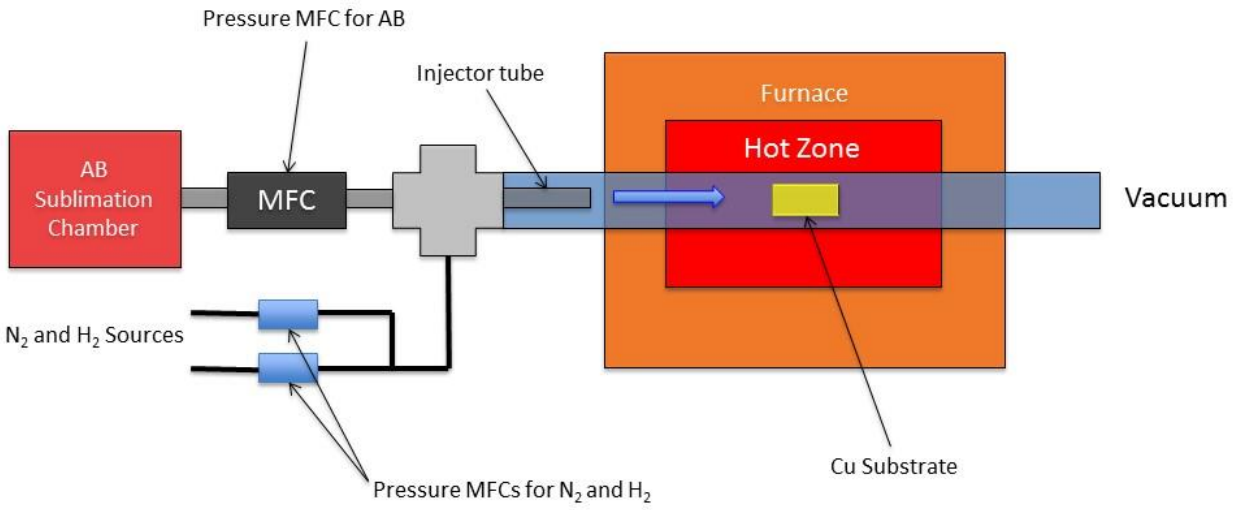

Figure 2.1.1 A schematic view of the CVD system used in in the growth of hBN. Ammonia borane was sublimated separately from the system and all gases were introduced into a cross-tube to mix before being introduced into the 'hot zone' of the system. The sample was located directly in the middle of the hot zone to insure maximum temperature; system was kept at ~10^{-2} Torr

The effects of substrate temperature, precursor sublimation temperature, pressure, exposure time, chemistry, and flow rates were studied; samples were characterized using Raman spectroscopy and scanning electron microscopy (SEM). For Raman spectroscopy, a 488 nm laser with a spot size of 331 nm was used while multiple SEMs were used.

2.2 Physical Vapor Deposition and Angular Resolved Photoelectron Spectroscopy of Tungsten Disulfide

All PVD WS_2 and additional CVD h-BN samples were prepared and examined *in-situ* under ultra-high vacuum ($<10^{-9}$ Torr) on single crystal Ni(111) and Pt(110). Samples were first sputtered with Ar, annealed with O_2 to remove C (common contaminant in transition metals), sputtered again to remove any oxide layer, and then annealed without O_2 in order to reconstruct the surface.

Tungsten was deposited by electron beam evaporation at 60 mA and 3 kV in a sulfur atmosphere on multiple surfaces at both 120°C and 400°C. Hexagonal boron nitride was deposited via chemical vapor deposition (CVD) in UHV using an ammonia borane precursor on both Ni(111) and Pt(110) at 700°C. Gold was also deposited via electron beam evaporation at 10 mA and 2 kV and thermal evaporation with a filament current of 85 A on Ni(111) and intercalated under h-BN at 400°C.

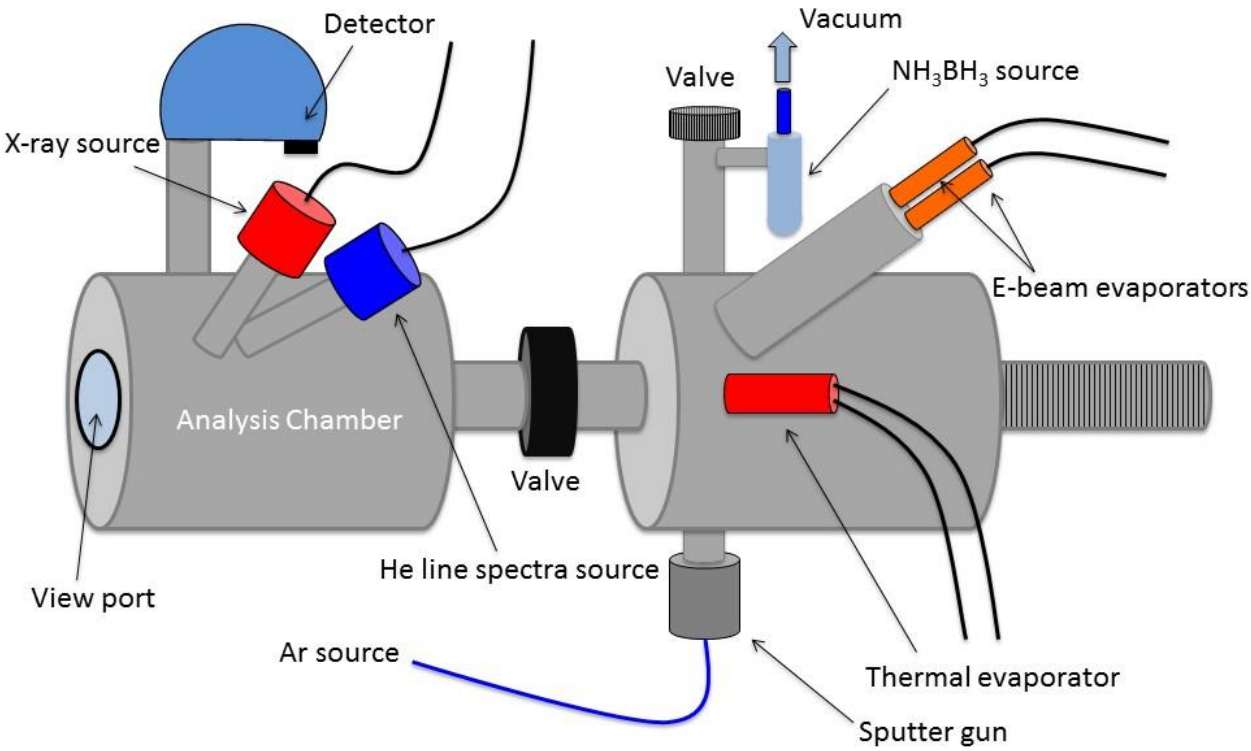

Figure 2.2.1 Illustrated image of preparation and analysis chambers used in PVD experiments. Preparation chamber regularly held under pressure ~2.0×10^{-9} mBar while the analysis chamber regularly achieved 8.0×10^{-10} mBar. All depositions and exposures occurred in preparation chamber and were completely separate from analysis chamber

Tungsten was calibrated so that deposition times yielded one monolayer of coverage while 5-10 layers of Au were deposited to sufficiently decouple the system from the Ni(111) substrate. The h-BN deposition was considered to be self-limiting and a deposition time of 10 minutes was used to insure complete coverage. Tungsten disulfide samples deposited at 120°C were annealed at 200°C, 300°C, and 400°C to monitor the transition from the metallic phase (1T) – of octahedral symmetry – to the semiconducting phase (2H) – of trigonal prismatic symmetry.[3]

All samples were characterized using low energy electron diffraction (LEED) to determine crystal structure, x-ray photoelectron spectroscopy (XPS) to determine core electronic structure, and ultraviolet photoelectron spectroscopy (UPS) to determine valence band structure. Epitaxial samples were also examined using angular resolved photoelectron spectroscopy to

investigate their valence band dispersion. Additionally, monolayer WS_2 was confirmed via Raman spectroscopy.

An illustrated image of the system used for deposition and characterization is shown above in Figure 2.2.1 and an illustrated image of the sample holder design is shown below in Figure 2.2.2.

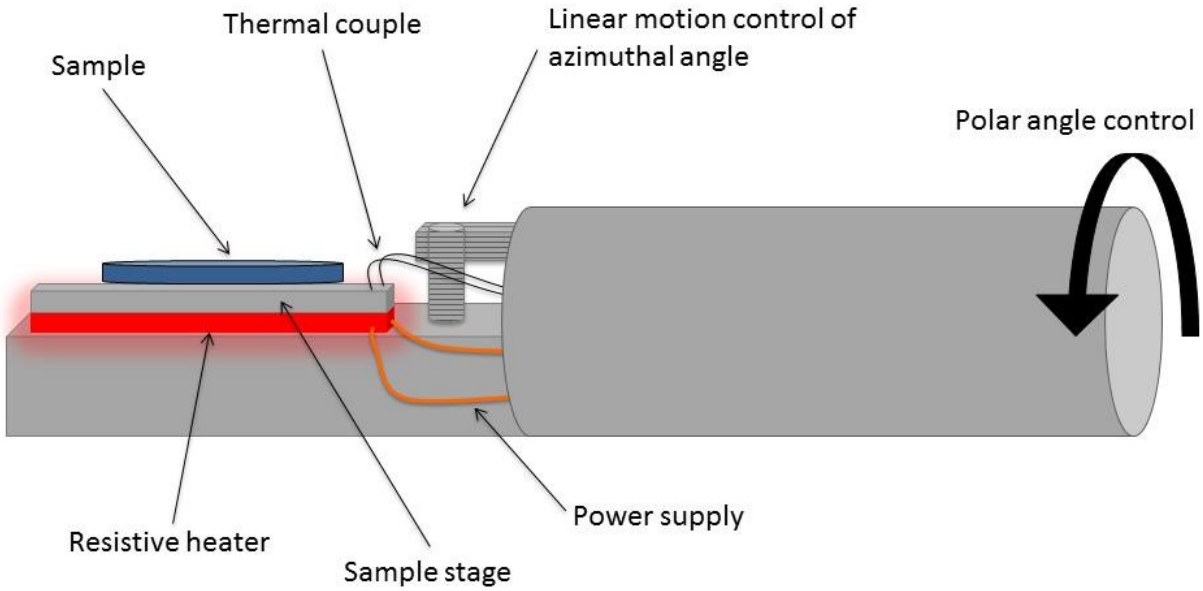

Figure 2.2.2 Illustrated image of the sample holder design where the azimuthal angle is controlled by a linear motion motor that rotates the sample stage while the polar angle is controlled by rotating the entire arm; The sample was heated resistively by a tungsten wire wrapped in Al_2O_3 coiled underneath of the Mo sample stage.

3 Growth of Hexagonal Boron Nitride

3.1 Hexagonal Boron Nitride Characteristics

Hexagonal boron nitride (h-BN) is an insulating isomorph of graphene. It has a bandgap of ~6 eV, in-plane thermal conductivity of 1700-2000 Wm/K, and a 2% lattice mismatch when compared to graphene; as a result, h-BN has attracted recent attention for integration into graphene electronics as well as other 2D electronics. It is a direct bandgap solid and can also be used for optoelectronic devices such as solar blind detectors and UV-lasers. Thus, this thesis

describes a CVD method to grow low defect density h-BN on Cu for integration into future electronics. The structure of h-BN is illustrated below in **Figure 3.1.1**.

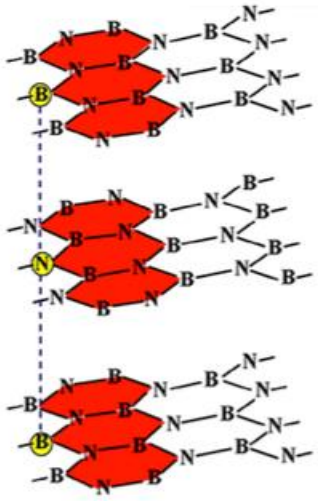

Figure 3.1.1 An illustrated structure of h-BN where it exhibits lattice parameters of $a = 2.50$ Å and $c = 2.66$ Å;[7,9] h-BN has an ABA stacking pattern where a B atom is overlaid by a N atom and where atoms in plane are strongly bound by covalent bonds while planes are loosely bound by van der Waal's bonding.[45]

Prior to this study, h-BN had been grown via CVD at ~1000°C ± 100°C using ammonia borane (NH_3BH_3) as a precursor chemical. The ammonia borane (AB), in all previous studies, was introduced to the system via a valve that was either open or closed with no control over flow rate. Thus this study serves to demonstrate the first quantitative study of the effect of AB flow rate on the growth of h-BN on Cu; it also examines the effects of growth temperature, pressure, sublimation time, and growth time.

Additionally, prior studies have reveal the growth of triangular h-BN domains on transition metal surfaces while one study has demonstrated the growth of hexagonal h-BN domains on very smooth transition metal surfaces. The formation of triangular domains is due to the thermodynamic stability of N terminated edges while the growth of hexagonal domains is favorable for integration with graphene devices due to the hexagonal grain structure of

graphene.[1,25,30,60] Thus this thesis will also examine the effect of growth on electropolished and non-electropolished surfaces.

Characterization of h-BN was done by Raman spectroscopy where a peak at 1370 cm^{-1} corresponds to monolayer h-BN and a shift to lower binding energy is indicative of multilayer h-BN.[7,61] This mode is a degenerate TO/LO and corresponds to out-of-phase oscillation of the B and N atoms as explained in the introduction. **Figure 3.1.2** illustrates the difference in Raman signature of monolayer and various multilayer systems as determined by Gorbachev *et al.*[61]

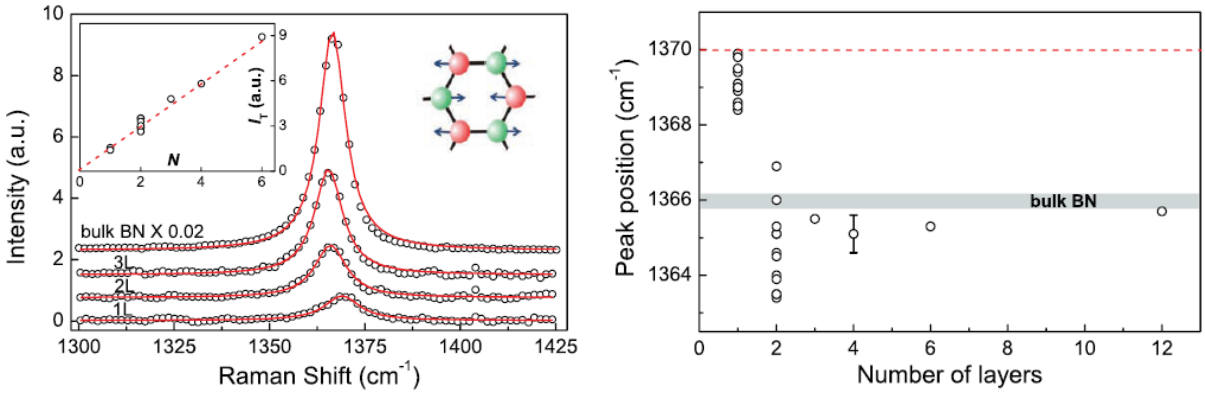

Figure 3.1.2 Graphical depiction of the changing Raman signature for h-BN monolayer and multilayer systems as a function of number of layers;[61] lower number of layers results in higher wavenumbers where monolayer systems are found at wavenumbers >1368 cm^{-1}.

3.2 Growth of Hexagonal Boron Nitride on Cu Substrates

The effects of flow rate were examined for AB, H_2, and N_2; AB is the reactive gas, H_2 is a reductant used to clean the surface of the Cu foil prior to deposition, and N_2 is an inert carrier gas. The flow rate of AB ranged between 1.5-5 sccm, the flow rate of H_2 ranged between 7-7.5 sccm, and the flow rate of N_2 ranged between 3-30 sccm. Growth times were generally between 5-10 minutes. Higher flow rates were not possible to quantitatively examine due to the inability to maintain a constant flow rate for >2 minutes of growth.

Table 3.2.1 Experimental parameters of first h-BN growth attempt where h-BN and C contamination were both observed; C contamination is a result of the high sublimating temperature and low thermal decomposition of the original o-rings used

Substrate	Deposition Temp. (°C)	Sublimator Temp (°C)	Pre-Growth Time (h)	Pressure (mTorr)	Growth Pressure (mTorr)	Flow Rate (N2/H2/AB)	Growth Time (mins)
Cu	1000	150	2	350	Start: 100 Finish: 100	30/7.5/5	10

Initial experiments explored growth of h-BN with a flow rate of 5 sccm AB. The Cu foil was annealed for two hours at 1000°C prior to deposition in order to grow the Cu grains and allow for reduction of the surface Cu oxide by flowing H_2 and N_2. Samples were placed in the front, middle, and back of the hot zone of the furnace to investigate where h-BN most efficiently grows. Fifteen minutes prior to starting the deposition, the sublimator temperature (T_{sub}) was slowly ramped to 150°C pausing to purge the hydrogen evolution associated with the thermal decomposition of AB. All experimental parameters are shown above in **Table 3.2.1** and will be presented this way hereafter for conciseness. After 2 hours of pre-growth anneal, the MFC was opened to allow 5 sccm of AB flow in the chamber while the N_2/H_2 respective flow rates were 30/7.5 sccm. Growth was 10 minutes at 1000°C and resulted in a Raman peak at 1371 cm^{-1} and a broad peak located at 1590 cm^{-1} convoluted on Cu fluorescence peak.

The peak at 1590 cm^{-1} is associated with C and is due to C contamination from sublimating o-rings in the system. Additionally, while all samples exhibited the C peak, only the central sample exhibited the peak at 1371 cm^{-1} due to h-BN. The offset of this peak could be attributed to the resolution of the Raman spectrometer being >1 cm^{-1}. It is also important to note that during this growth, ripples on the Cu surface were observed likely due to melting and recrystallizing of the Cu; this is shown below in **Figure 3.2.1** along with the observed Raman spectra.

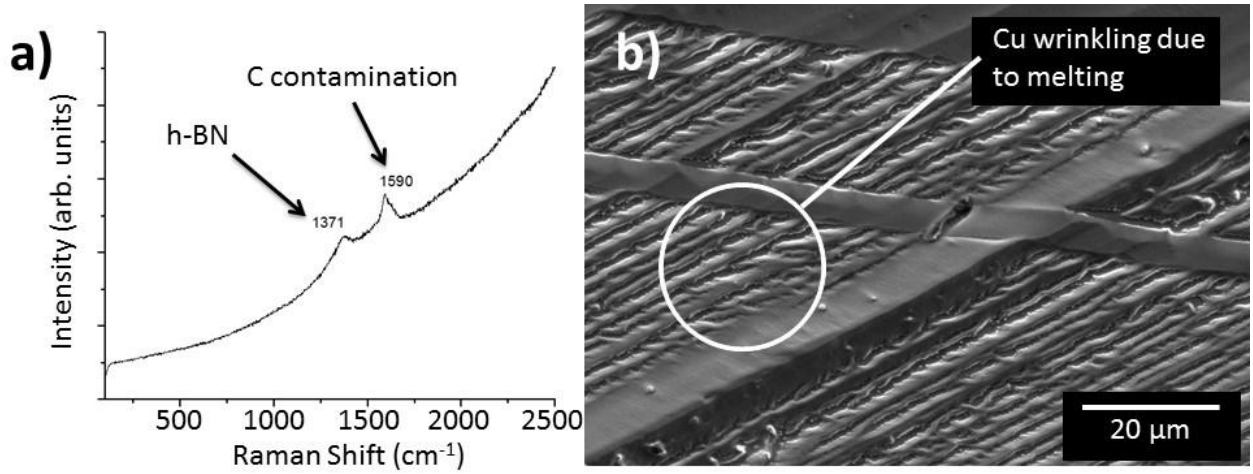

Figure 3.2.1 Characterization of first h-BN growth attempt **a)** Raman spectrum where peak at 1371 cm^{-1} corresponds to monolayer h-BN and peak at 1590 cm^{-1} corresponds to C contamination from o-rings **b)** SEM image of Cu ripples due to melting of surface, no h-BN triangles were observed anywhere on sample

The second experiment investigated the effects of increased pressure in the system; where the first experiment was conducted at 350 mTorr, the pressure was doubled to 700 mTorr. Parameters for this experiment are outlined below in **Table 3.2.2**. It should be noted that while sublimator start and end pressures are listed for each experiment, the goal was to maintain a sublimator pressure of 100 mTorr from start to end; however, due to unbalanced, non-linear sublimation rate of AB inside of the chamber and the flow rate of AB out of the chamber, this was often difficult to maintain.

Table 3.2.2 Experimental parameters for h-BN growth at 700 mTorr

Substrate	Deposition Temp. (°C)	Sublimator Temp. (°C)	Pre-Growth Time (h)	Pressure (mTorr)	Growth Pressure (mTorr)	Flow Rate (N2/H2/AB)	Growth Time (mins)
Cu	1000	150	2	700	Start: 130 Finish: 100	30/7.5/5	10

For this experiment, a Raman signature at 1374 cm^{-1} was observed and dark spots were observed under optical microscopy (OM) on the Cu surface; it is interesting to note that no C signal was observed during this experiment. SEM was also conducted and observed similar Cu ripples on the surface; *in-situ* electron diffraction spectroscopy (EDS) was conducted in order to

determine the exact content of the ripples. It was found that the ripples are Cu; because B and N both have very low sensitivity in EDS they not detected, however, there is no SEM evidence to suggest h-BN on the surface. Carbon though, which can be detected via EDS was not observed. Again, no h-BN triangles were observed under SEM; the characterization results of test 2 are found below in **Figure 3.2.2**.

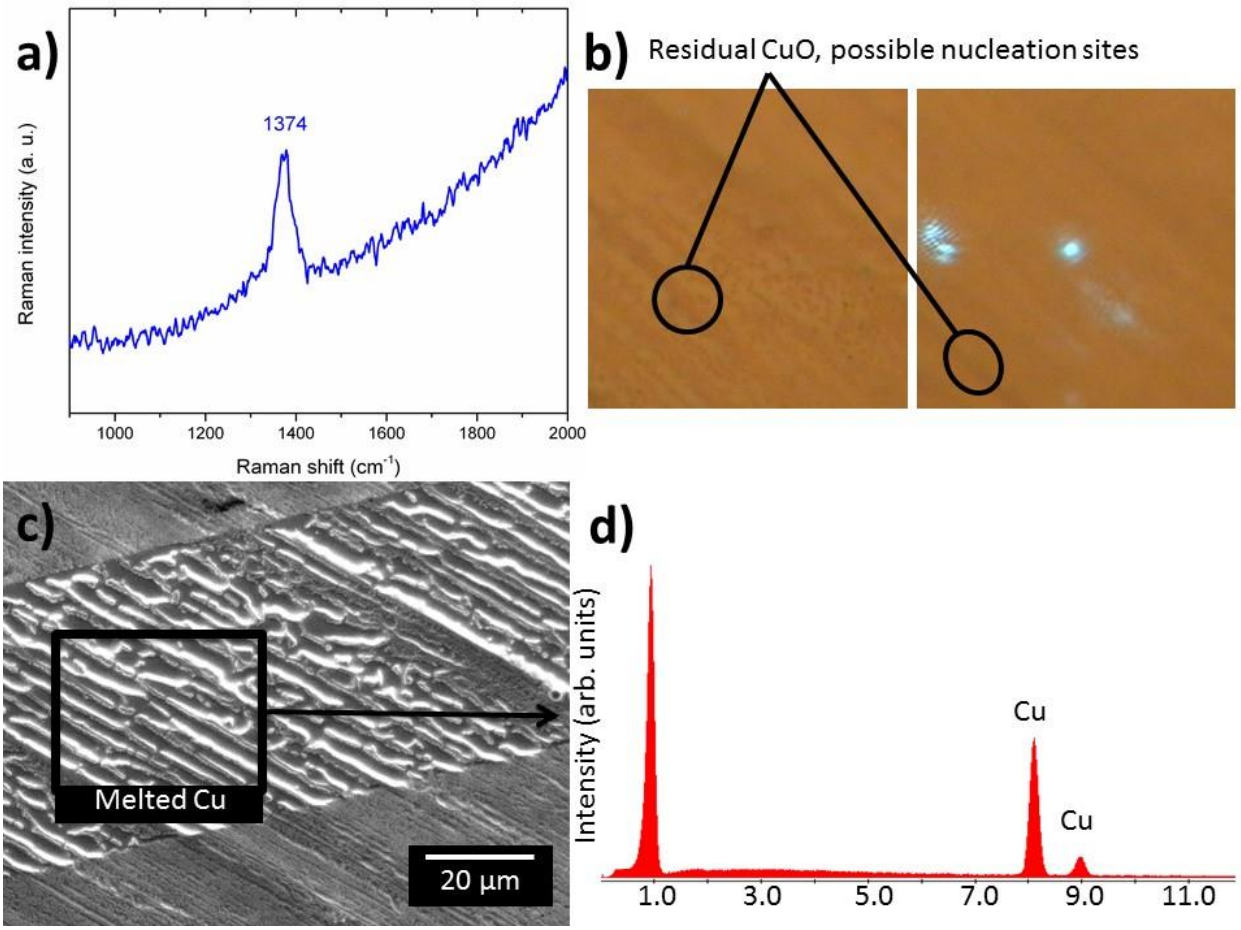

Figure 3.2.2 characterization of h-BN growth trial at 700 mTorr **a)** Raman spectrum where peak at 1374 cm^{-1} could indicated h-BN growth **b)** OM images of Cu foil during Raman spectroscopy showing discolorations on the surface, likely due to incomplete cleaning of oxide surface pregrowth **c)** SEM image of Cu ripples on surface **d)** EDS scan on Cu ripples

Due to the consistent appearance of Cu melting during growths, the furnace was recalibrated and growth parameters were adjusted to eliminate Cu melting. Initial growths following the calibration continued at 1000°C but were eventually increased to 1050°C due to

thermal conduction and an observed difference between set temperature and actual temperature in the furnace hot zone.

The initial growth after recalibration was identical to trial 2, however this time an electro-polished Cu substrate was used instead of a mechanical polished substrate. Electro-polishing the substrate reduces the root-mean-square (RMS) roughness and creates a smoother surface with a decreased defect density than that of mechanically polished Cu. Because it is hypothesized that h-BN preferentially grows on surface defects, similar to graphene, by reducing the defect density on the surface, it is expected that nucleation of h-BN domains should decrease. As a result, domains that do nucleate would thus be able to grow larger.

Trial 3 used the parameters outlined above in **Table 3.2.2** and yielded a very small Raman signature at 1375 cm^{-1}. SEM showed a material that was charging located on top of a large Cu defect with no apparent order. This is the first observed example (via SEM) of any insulating layer being deposited by this process. The Raman spectrum and SEM of the insulating material can be found below in **Figure 3.2.3**.

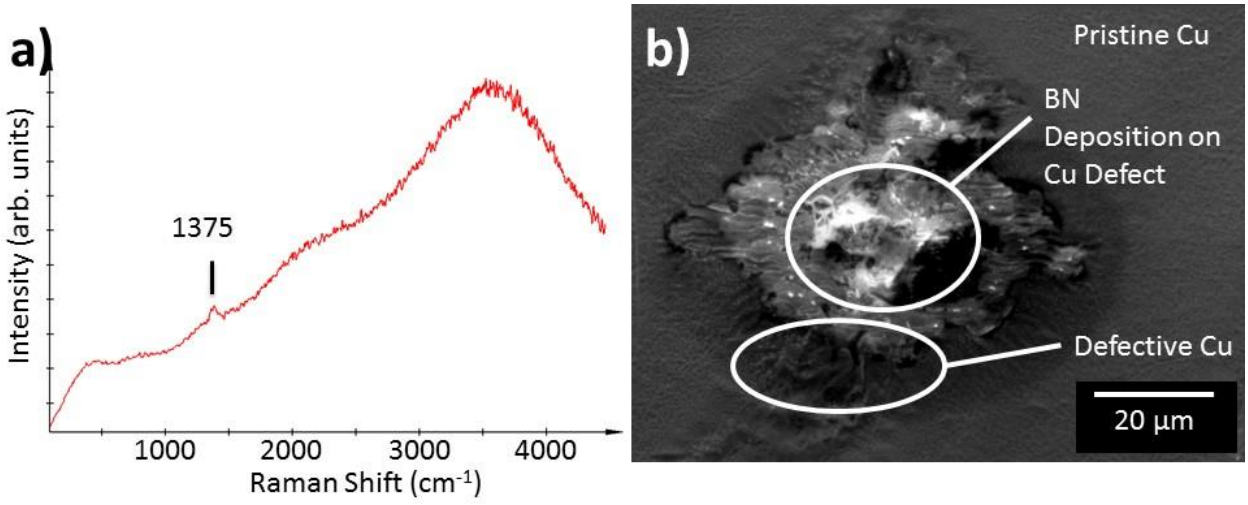

Figure 3.2.3 Characterization of h-BN growth trial on electro-polished Cu foil at 700 mTorr **a)** Raman spectrum where a small peak at 1375 cm^{-1} is observed convoluted on Cu fluorescence peak **b)** SEM of large Cu defect with charging in the center likely due to the presence of an insulating layer

Due to inconclusive results and additional literature review, multiple growth parameters were changed. The furnace temperature was increased to 1070°C, the sublimation temperature was decreased to 120°C with a longer ramp time, the flow rate of N_2 was increased to 40 sccm, and the growth time was decreased to 6 minutes. Electro-polished Cu was used again; however, the results yielded Raman signature at 1351 cm^{-1} and a strong peak at 1590 cm^{-1} indicating C contamination. At this point the furnace was disassembled, cleaned, and the o-rings replaced with high temperature o-rings.

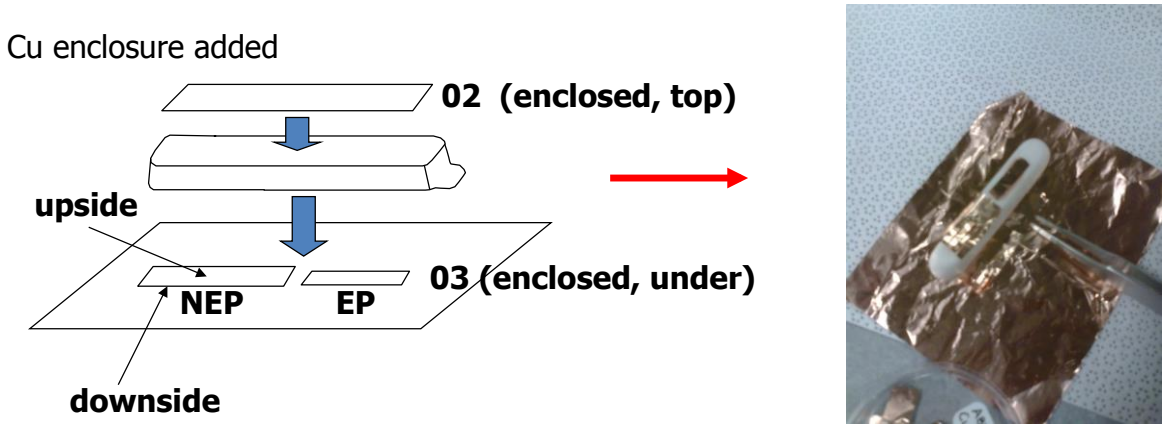

Figure 3.2.4 A schematic (left) and image (right) of the Cu enclosure used to limit the AB flow over the Cu substrates where substrate positions are shown for the first trial

The first h-BN was seen when the flow of AB was limited by introducing a wrapped ceramic boat enclosure into the system as illustrated above in Figure 3.2.4 and reducing the N_2 flow rate. Experimental parameters can be found below Table 3.2.3. Two samples – one electro-polished and one not – were enclosed under an alumina boat, which was then wrapped in unpolished Cu foil. Monolayer h-BN triangular domains were observed on the electro-polished Cu while some domains similar in size were observed with increased thickness as demonstrated in Figure 3.2.5; Domains observed achieved sizes of $5 - 10\ \mu m$ while multilayer domains rarely exceeded $500\ nm$. In some cases, sections of multilayer h-BN are observed in isolated areas on

monolayer domains likely as a result of vertical propagation of defects. The nucleation density observed was high thus limiting the domain size. The top facing side had larger domains and larger nucleation density as compared to the bottom facing side; additionally the non-electro-polished sample exhibited high defective growth with an even high nucleation density.

Table 3.2.3 Deposition parameters for the first observed h-BN and following experiments to determine optimal substrate/substrate placement

Substrate	Deposition Temp. (°C)	Sublimator Temp. (°C)	Pre-Growth Time (h)	Pressure (mTorr)	Growth Pressure (mTorr)	Flow Rate (N2/H2/AB)	Growth Time (mins)
Cu	1050	N/A	2	700	N/A	3/7/3	10

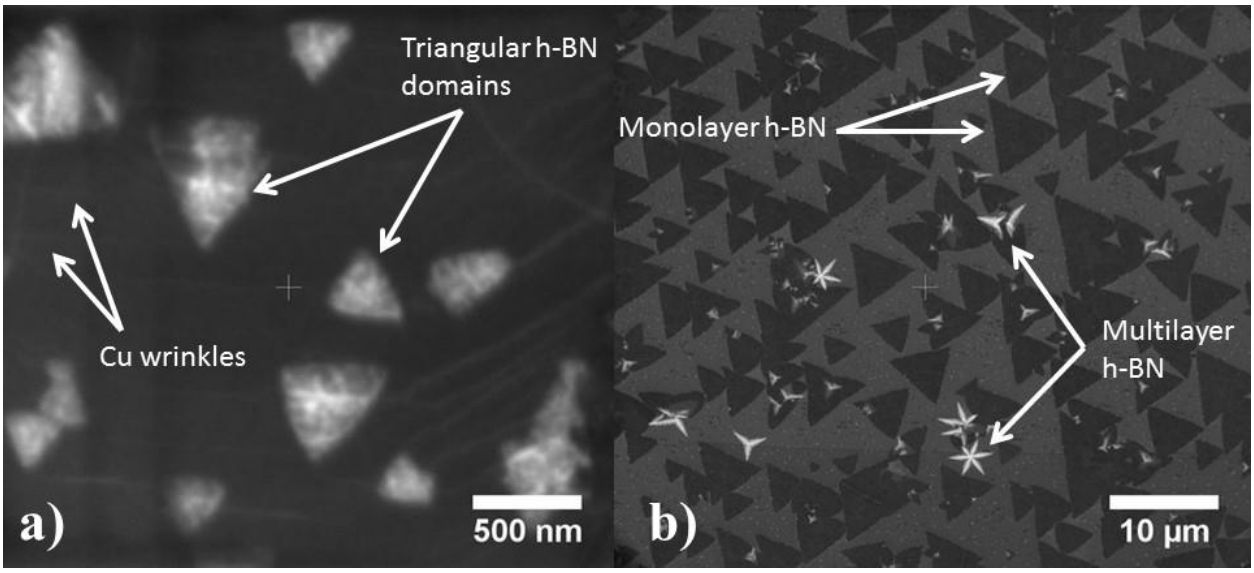

Figure 3.2.5 SEM images of h-BN on Cu electro-polished Cu foil **a)** small multilayer domains located on top of a monolayer domain **b)** high nucleation density of h-BN domains where some star shaped charging phase is observed; some monolayer domains have small multilayer domains on top

Cu foil outside of the boat had particulates similar to those shown for previous growths. Foil located closer to the AB source was highly coated with an insulating material as indicated by charging while foil located far away from the AB source was not coated. Consequently, it is evident that sample location in the furnace is important due to AB consumption.

The experiment was repeated with three electro-polished samples distributed evenly under the ceramic boat and, interestingly, a reduced domain size ($1\ \mu m - 2\ \mu m$) was observed. Again a high nucleation density was found; additionally, a high concentration of wrinkles on the surface of all h-BN domains was observed, possibly due to a difference in thermal coefficients of expansion between the h-BN and Cu foil. Using the same parameters and reusing the enclosure, coalescence between triangular domains was observed in limited cases. However, the substrates were not uniformly coated; some sections demonstrated monolayer domain coalescence while other areas of the substrates demonstrate isolated, multilayered domains. This is likely a consequence of AB consumption, substrate position, and mass transfer within the furnace.

To reduce nucleation density, the flow rate of AB was reduced to 1.5 sccm. However, this yielded a limited number of triangles, primarily multilayered, and nanoribbons. The ribbons form along grain boundaries of the Cu foil due to reduced energy of formation. In some cases the domains are broken and folded. The observed triangles formed in lines and coalesced. The formation is along ripples in the Cu substrate. This phenomenon can be seen below in Figure 3.2.6a where the h-BN domains formed along ripples appear to be faintly lighter than the substrate.

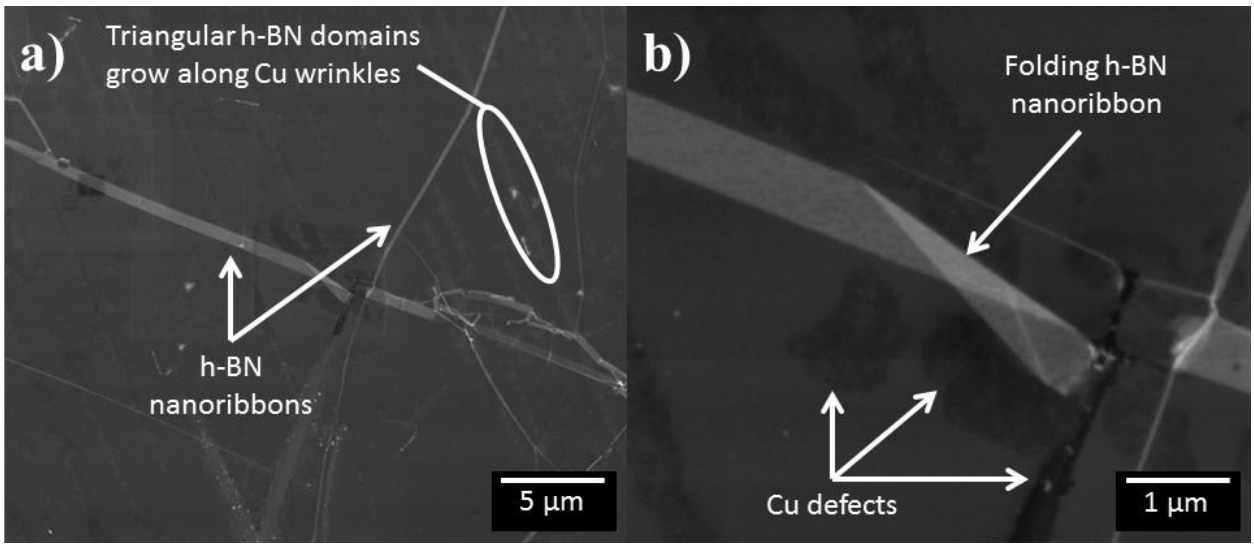

Figure 3.2.6 SEM images of h-BN grown in ceramic enclosure with AB flow rate of 1.5 sccm **a)** low magnification image of ribbon formation along Cu grain boundaries and triangle domains along Cu wrinkles **b)** broken and folded ribbon with low on a highly defective surface

3.3 Growth of Hexagonal Boron Nitride in Ultrahigh Vacuum

Hexagonal boron nitride was also grown Pt(110) and Ni(111) single crystals in UHV by CVD. Due to the greatly reduced pressure, h-BN growths were possible at temperatures as low as 630°C. Samples were first grown on a Pt(110) crystal at 630°C and 730°C by dosing NH_3BH_3 for ten minutes and characterized by XPS and ARPES.

As expected, growth at 730°C yielded better-defined bands in ARPES due to increased mobility of atoms on the surface and thus increased crystallinity; however, the N 1s XPS emission line is convoluted with the Mo 3p 3/2 line, shown in Figure 3.3.1b. Because of the small size of the Pt(110) crystal used, detection of residual signal from the Mo sample holder is unavoidable. Interestingly, h-BN grown at 630°C demonstrates stronger XPS characteristics, located closer to previously reported values for h-BN, though the measured ARPES is relatively diffuse. Though it appears that a lower energy band may be visible in the 630°C band dispersion, it is unlikely that this is a band due to the low quality of the growth. Rather it is more likely that this artifact is a result of band smearing due to a large amount of edge defects – a consequence of the small grains. The overall XPS and ARPES measurements indicate higher coverage but reduced film quality. It is possible that the decreased temperature increased the condensation of BN particles from the vapor phase; however, due to the reduced surface mobility, these particles would have had less energy to diffuse along the surface and further react to create large domains.

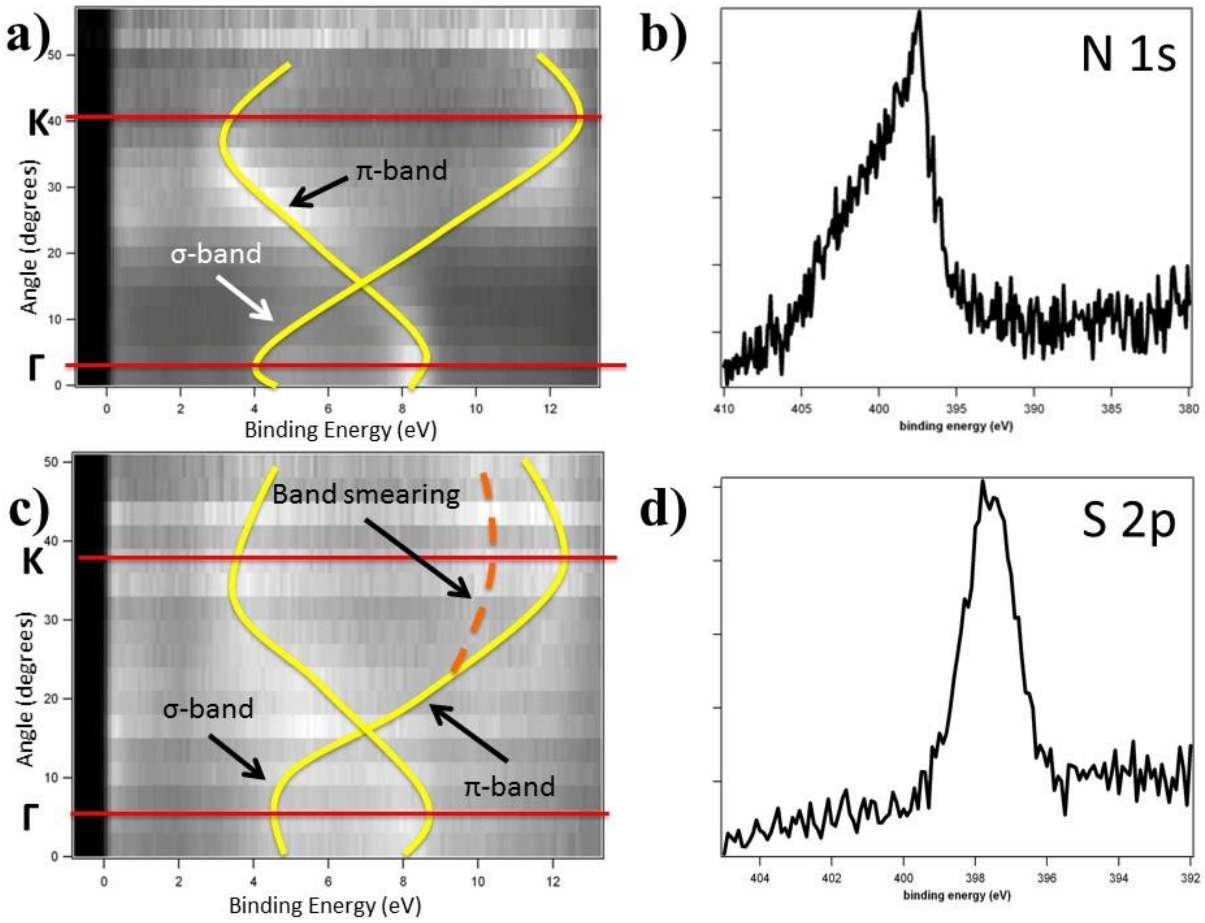

Figure 3.3.1 XPS and ARPES of h-BN grown on a Pt(110) single crystal **a)** ARPES of growth at 730°C **b)** XPS N 1s emission line convoluted with Mo 3p 3/2 for growth at 730°C **c)** ARPES of growth at 630°C **d)** XPS N 1s emission line for growth at 630°C

The scanned crystallographic direction was determined originally by LEED and then confirmed by ARPES. The Γ direction is measured by normal emission while scanning from the center (0,0) point of LEED to an adjacent blurred 2x1 point of the Pt(110) which indicates K or X direction depending on epitaxy. After ARPES measurements were made, the angular difference between directions was calculated using equation below:

$$hk_{\parallel} = \sqrt{2m_e E_{kin}} \sin\theta$$

Where $k_{\parallel}$ is the momentum parallel to the sample surface, m_e is the mass of an electron, E_{kin} is the measured kinetic energy of the electron and θ is the measured angle; therefore $\Gamma - K = 30.2°$ and $\Gamma - X$ was calculated to be less ($\sim 28°$); because the measured angular difference between

the Γ direction and subsequent maximum was $\sim 32 - 34°$ in both cases, it was thus determined that the scans were made in the $\Gamma - K$ direction. This conclusion is consistent with the band diagram measured by Nagashima *et al.* though not all bands are resolved due to limitations of the detector.[10]

4 Growth and Characterization of Tungsten Disulfide

Tungsten Disulfide (WS_2) was grown on Ni(111), Au/Ni(111), h-BN/Ni(111), and h-BN/Au/Ni(111). It was grown by e-beam evaporation of tungsten in a sulfur atmosphere at 10^{-8} mBar. Growth and characterization were performed *in-situ* in UHV; all samples were characterized by x-ray photoelectron spectroscopy (XPS), ultraviolet photoelectron spectroscopy (UPS), low energy electron diffraction (LEED), and, in some cases, verified with Raman spectroscopy. The effects of growth temperature and annealing were investigated in order to better understand the metallic to semiconductor transition.

Before growths, the Ni(111) single crystal was cleaned via Ar sputtering at 10^{-5} mBar and then annealed in O_2 at 700°C for 1 minute to alleviate C content. Because it was common for NiO to form during this step (as characterized by LEED), a second round of Ar sputtering was used and a second anneal without O_2 at 700°C was used in order to achieve a (111) surface construction.

4.1 WS_2/Ni(111)

First, WS_2 was grown on bare Ni(111) single crystal at 400°C. It is clear via XPS that both Wand S are present in the sample as illustrated in **Figure 4.1.1**a. It should be noted that the W 4f peaks were used to characterize the presence of WS_2 phases as is common in previous studies. The integrated intensity of the W 4f peak is consistent with ~1 monolayer (ML) which

was determined by *in-situ* calibration immediately prior to this experiment. Sulfur also exhibits a relatively intense peak suggesting full coverage of the W-S species. Peak positions of the W 4f 7/2 and 5/2 respectively were 32.3 eV and 34.5 eV which is consistent with 2H-WS_2 as demonstrated in **Figure 4.1.1**b.

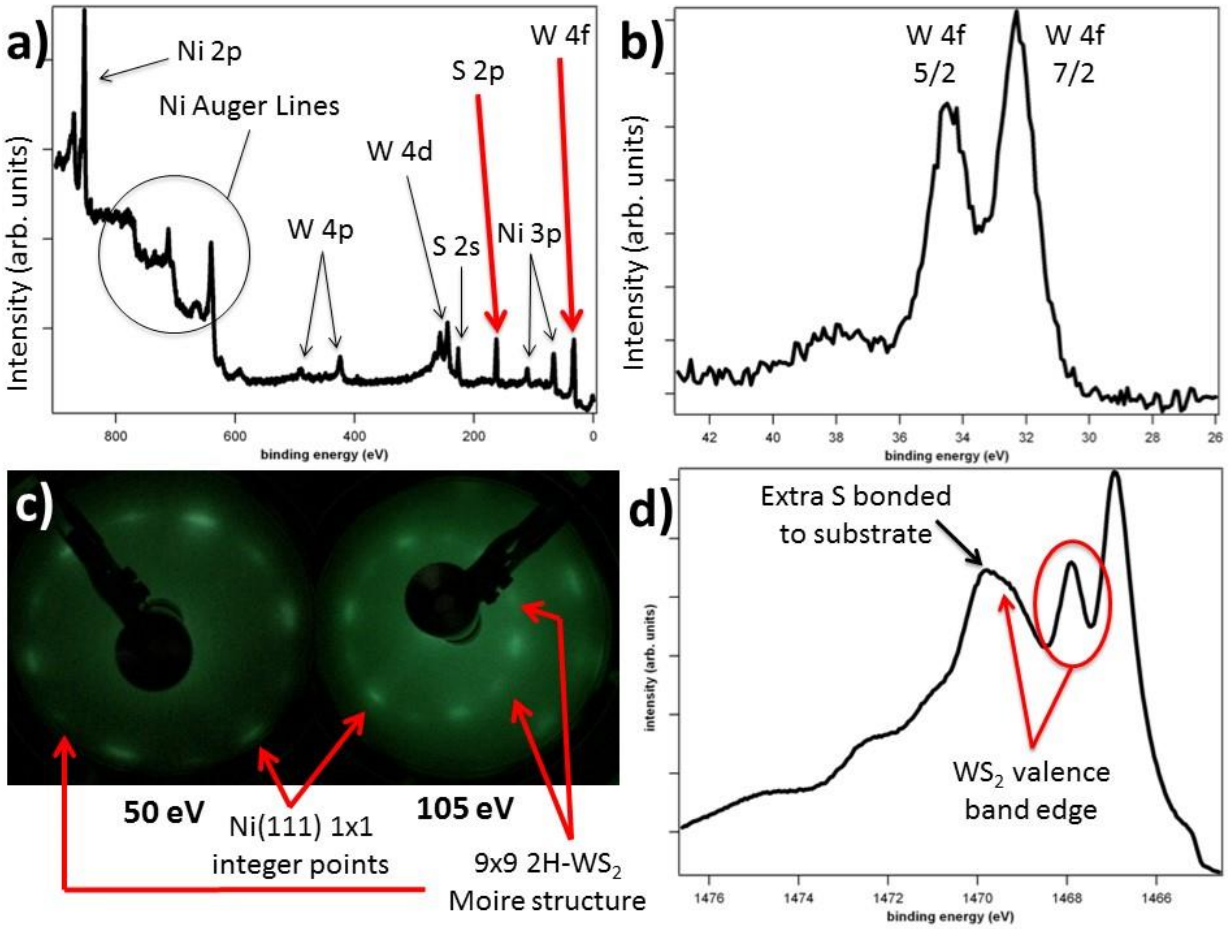

Figure 4.1.1 Characterization of WS_2/Ni(111) single crystal **a)** XPS survey with pass energy (PE) of 50 **b)** XPS scan of W 4f at PE20 shows the splitting of the W 4f 7/2 and 5/2 peaks **c)** 9x9 LEED of WS_2/Ni(111) where the more intense spots are those of the Ni(111) and the less intense spots are those of 2H-WS_2; radial blurring suggests high strain **d)** He-I UPS spectra at PE2 of WS_2/Ni(111) where the first peak at the Fermi edge is the metallic edge of Ni(111) and the sharp peak located in the foot, 1.7 eV from the Fermi edge is the σ-band of 2H-WS_2

LEED suggests the formation of an epitaxial layer on the Ni(111) surface. Where the original Ni(111) surface demonstrates a 1x1 construction, the addition of W and S resulted in a radially blurred 9x9 construction as demonstrated in **Figure 4.1.1**c. It appears that the 1x1

construction of the Ni(111) is still visible while there is an additional 30° rotated 1x1 structure due to the WS_2; both of these likely add together to generate the 9x9 observed super-structure. The radial blurring suggests an epitaxial construction with high strain.

UPS, shown in **Figure 4.1.1**d, demonstrates the generation of new bands with respect to bare Ni. The first, broad band-edge located at the Fermi edge and continuing ~1.5 eV is the metallic band edge of the Ni substrate; however, the well-defined band located in the foot of the metallic band, 1.7 eV is the σ-band of 2H-WS_2. The π-band can be found 3.9 eV from the Fermi edge and is partially convoluted with another band that is likely due to S adhered to the transition metal surface. Finally, Raman spectroscopy confirmed the existence of 2H-WS_2.

4.2 WS_2/Au/Ni(111)

Next, WS_2 was grown on Au/Ni(111) where the Au was e-beam evaporated or thermally evaporated onto the surface. All experiments used 5-10 ML of Au to sufficiently decouple the WS_2 from the Ni(111) layer. Au was deposited at 400°C while WS_2 was deposited at 120°C and then annealed at 200°C, 300°C, and 400°C for 30 minutes; with each anneal, samples were examined via XPS and UPS. LEED for this sample is not shown because deposition at 120°C yielded what is likely an amorphous structure and thus no LEED pattern was discernable.

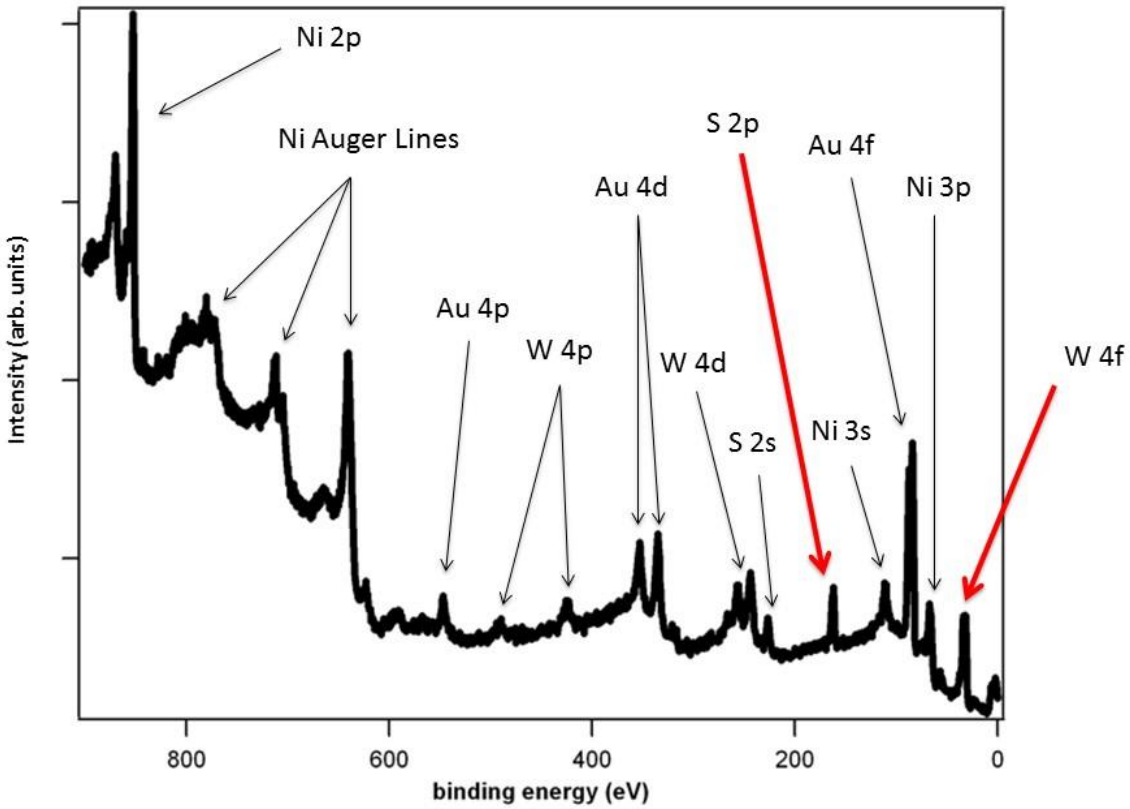

Figure 4.2.1 XPS survey at PE50 of WS_2/Au/Ni(111) deposited at 120°C where it is evident that there is less W and S content when compared to WS_2/Ni(111) deposited at 400°C

The XPS survey, shown in **Figure 4.2.1**, revealed decreased W and S content for the WS_2 deposited at 120°C, which is likely due to decreased adherence to Au as compared to Ni which strongly couples with the WS_2. Additionally, the position of the W 4f 7/2 and 5/2 peaks are respectively located at 31.7 and 32.2 eV; both significantly lower than on Ni(111) at 400°C. Most importantly though is the lack of any band ~1.7 eV from the Fermi edge visible in UPS.

As the sample was annealed, the W 4f peaks shifted to higher binding energy while the band located 1.6 eV from the Fermi edge developed and then increased in intensity. Both changes are illustrated in figure **Figure 4.2.2**a. It is important to note that there was very little change in both XPS and UPS for the 200°C anneal while annealing at 300°C realized a noticeable shift in the W 4f peaks as well as the development of the σ-band 1.7 eV from the

Fermi edge. Further annealing at 400°C further shifted the W 4f peaks and increased the signal of the σ-band. These trends are shown below in **Figure 4.2.2**b.

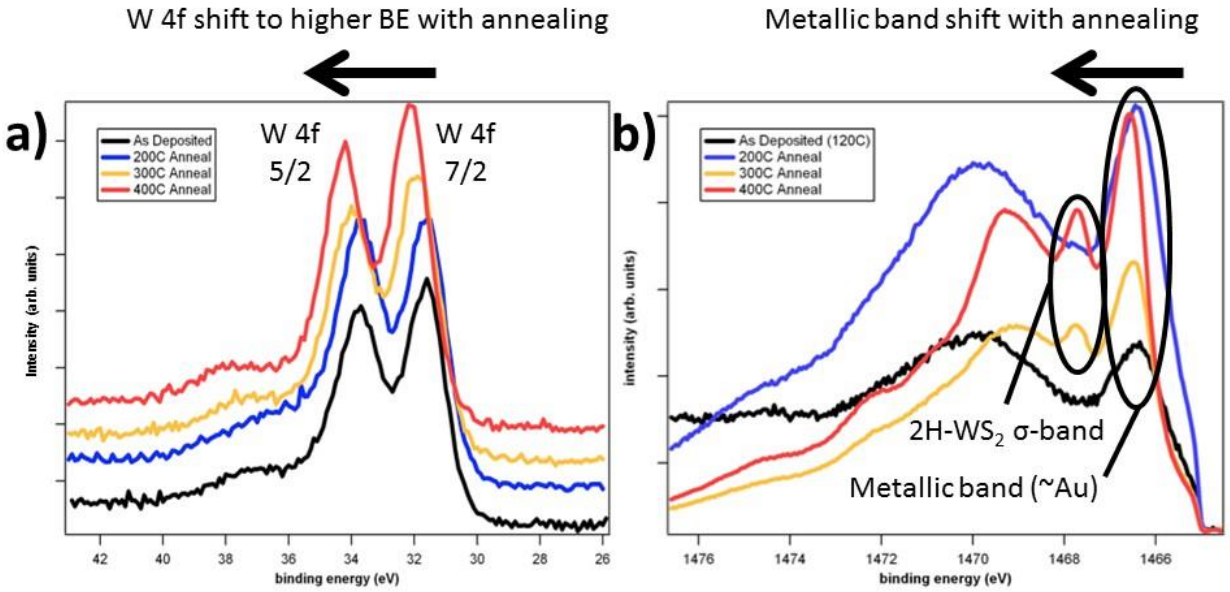

Figure 4.2.2 Evolution of WS_2 with annealing **a)** XPS PE20 of W 4f 7/2 and 5/2 peaks shifting to higher BE with annealing **b)** Evolution of He-I UPS at PE2 of WS_2 with annealing where the generation of the σ-band is found for annealing at 300°C

Valence band spectra artifacts were than matched to calculated orbital hybridizations. As shown below in **Figure 4.2.4**; $\Gamma_1^+, \Gamma_2^-, \Gamma_3^-$, and an additional Γ_1^+ are observed in the spectrum shown in **Figure 4.2.3**. These states are a result of hybridization between W $5d$ and S $3p$ orbitals. In TMDs there is a pronounced hybridization between metal d orbitals and chalcogenide p orbitals. Particularly, in WS_2 the valence band maximum is a result of d_{z^2} and p_z (Γ_1^+ *and* Γ_2^-) hybridization. Mixing of atomic orbitals in a reduced representation of the $P\bar{6}m2$ space group are shown in **Figure 4.2.4** along with their calculated positions in the UPS spectra, as shown in **Figure 4.2.3**. The evolution of the Γ_1^+ state was used to characterize the onset of semiconduction dominance in phase composition.

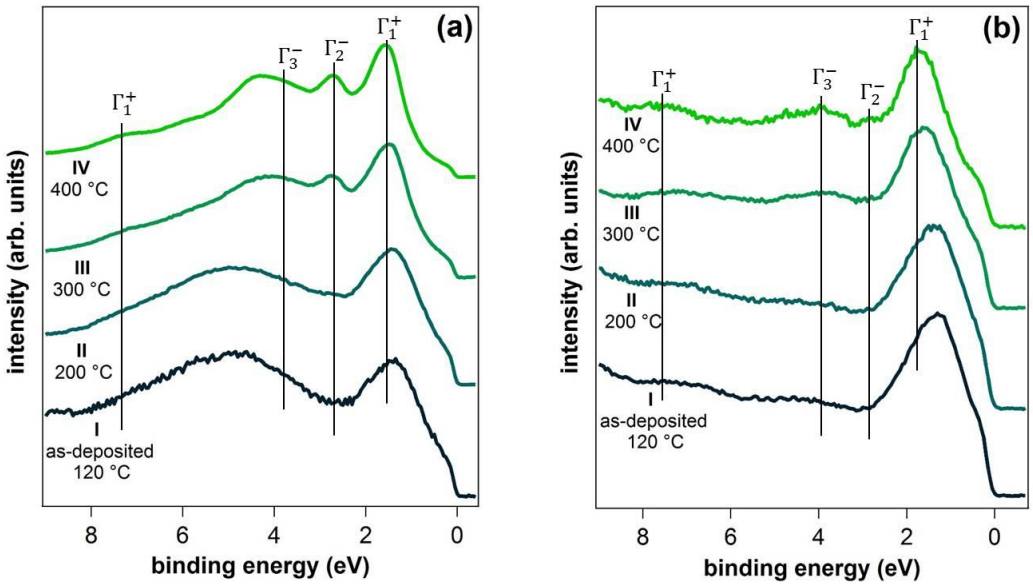

Figure 4.2.3 Evolution of valence band spectra of WS_2/Au/Ni(111) from as deposited (120°C) to 400°C annealing where the mixing of W and S orbitals are highlighted **a)** He-I PE2 **b)** He-II PE10

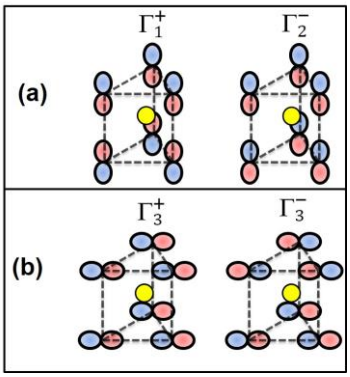

Figure 4.2.4 Possible combinations of **a)** p_z and **b)** p_x / p_y orbitals in monolayer 2H-WS_2 where symmetry labels used are for irreducible representations of the space group $P\bar{6}m2$

To quantitatively characterize the amount of 2H-WS_2 and 1T-WS_2 present in the system, the W 4f peaks were fit with Gaussian curves where the initial positions were set using previously reported values. The W 4f peaks were shifted respectively by normalized the Au 4f 7/2 peak to 84 eV. The peaks were then fit by considering a Shirley background and fitting the 2H, 1T, and convoluted W 5p peaks; the results are illustrated for all annealing in **Figure 4.2.5**.

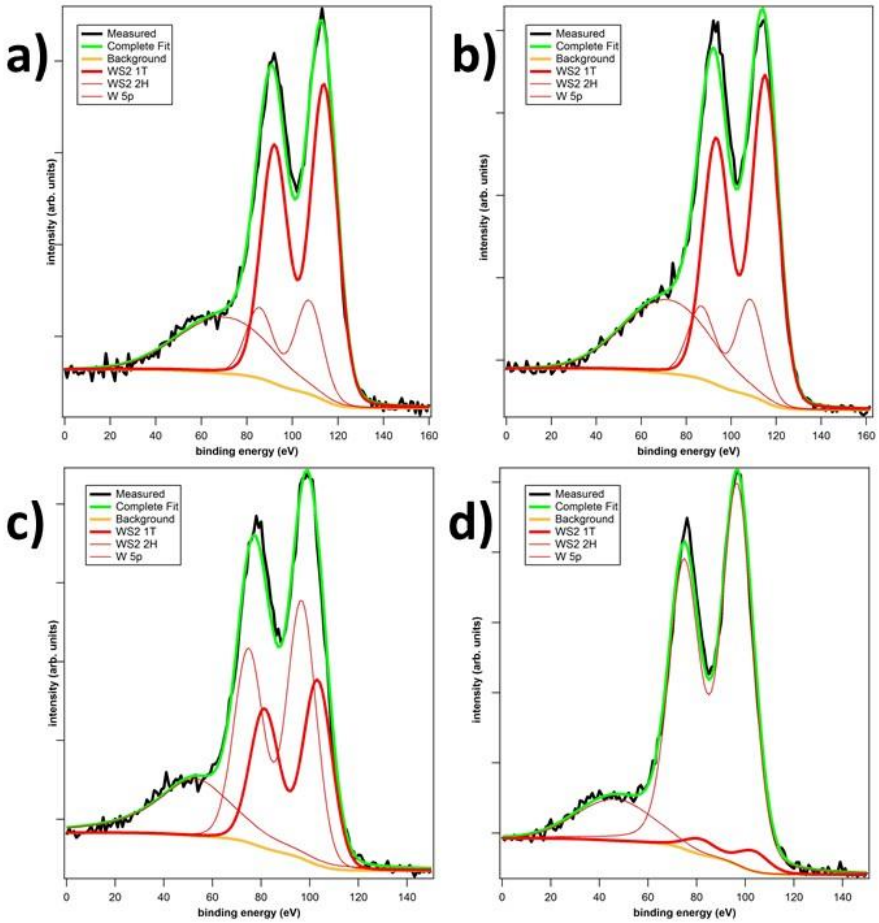

Figure 4.2.5 Fitted XPS of W 4f 7/2 and 5/2 peaks for **a)** as deposited at 120°C where the sample is primarily composed of 1T-WS_2 **b)** annealed at 200°C with little change **c)** annealed at 300°C where the phase transformation from 1T to 2H can be seen to begin **d)** annealed at 400°C and almost entirely transformed to 2H-WS_2

It was found that as deposited (120°C) WS_2 was primarily metallic and 1T-like in character while with subsequent annealing, the relative composition of 1T-like-phase decreased until at 400°C the sample was almost entirely 2H. Again, it is worth noting that there is very little difference between the as deposited phase and the phase present after annealing at 200°C. The most profound change occurs when annealing at 300°C where the sample begins to transform from primarily 1T-like to roughly half 1T-like and half 2H. Thus, this suggests that the transformation temperature between phases exists somewhere between 200°C-300°C; however,

due to the incomplete transformation, it is likely closer to 300°C. As expected, further annealing >300°C results in complete transformation to 2H-WS_2.

Tables outlining the calculated composition of 1T and 2H WS_2 are demonstrated below in **Table 4.2.1** and **Table 4.2.2** where values calculated by fitting the W 4f and S 2p peaks can be found. The S 2p peak was highly convoluted and demonstrated multiple degrees of freedom that were not analytically fixed; thus, the S 2p peaks cannot be analyzed quantitatively but the qualitative agreement that 1T transforms to 2H with increased annealing substantiates what was found using W 4f fits. Additionally, the consideration of WS_3 formation is also demonstrated in these tables and was found to remain almost constant with annealing.

Table 4.2.1 Calculated values for WS_2 phase composition as calculated by the W 4f peak integrated intensities

Annealing temperature (°C)	Area components				Total Area	Fractional area				2H/(1T+2H)*100
	1T 31.64	2H 32.32	WS3 33.58	5p		1T	2H	WS3	5p	
120	1765	722.5	320	265	3073	57.44	23.50	10.41	8.640	29.03
200	2031	785	398	488	3702	54.86	21.20	10.75	13.18	27.87
300	1236	1744	288	503	3771	32.78	46.24	7.637	13.34	58.52
400	336	2902	345	318	3901	8.61	74.39	8.843	8.15	89.62

Table 4.2.2 Calculated values for WS_2 phase composition as calculated by the S 2p peak integrated intensities. It is important to note that due to convoluted peaks and many degrees of freedom that could not be analytically set, the S 2p trends are strictly qualitative

Annealing temperature (°C)	Area components			Total Area	Fractional area			2H/(1T+2H)*100
	1T 161.67	2H 162.24	WS3 163.45		1T	2H	WS3	
120	846	577	234	1657	51.05	34.82	14.12	40.54
200	628	705	255	1588	39.54	43.40	16.05	52.88
300	560	938	235	1733	32.31	54.13	13.56	62.62
400	359	1359	214	1932	18.58	70.34	11.07	79.10

It was found that the as deposited system at 120°C had stoichiometry $WS_{2.9}$. This hyperstoichiometry was reduced to $WS_{2.5}$ with annealing to 400°C. It is likely that the additional sulfur content is a result of thermodynamically stable S terminated edges, S adherence to exposed transition metal surfaces, and adventitious S inadvertently deposited due to chamber contamination.

To obtain a reasonable LEED pattern, WS_2 was deposited at 400°C to provide increased mobility to atoms on the surface and therefore is able to attain the more ordered, energetically stable phase. W 4f photoemission lines for high temperature depositions yield highly separated peaks where the majority component can be attributed to 2H-WS_2. The corresponding LEED pattern is reported in **Figure 4.2.6**a and shows six elongated spots that form a hexagonal cell that corresponds to an incommensurate but azimuthally ordered 2H-WS_2 film. It is important to note that for low WS_2 coverage various S/Au reconstructions are observed. S can form multiple complex structures on Au surface where small temperature variations can cause different structure formations. No LEED pattern was observed for WS_2 deposited at 120°C due to the primarily amorphous structure as evident in the Raman spectra found in **Figure 4.2.6**b. Although 2H components can be observed, due to the lack LEED and metallic nature of the valence band spectra, the components can be attributed to nanocrystalline seed crystals surrounded by primarily amorphous WS_2.

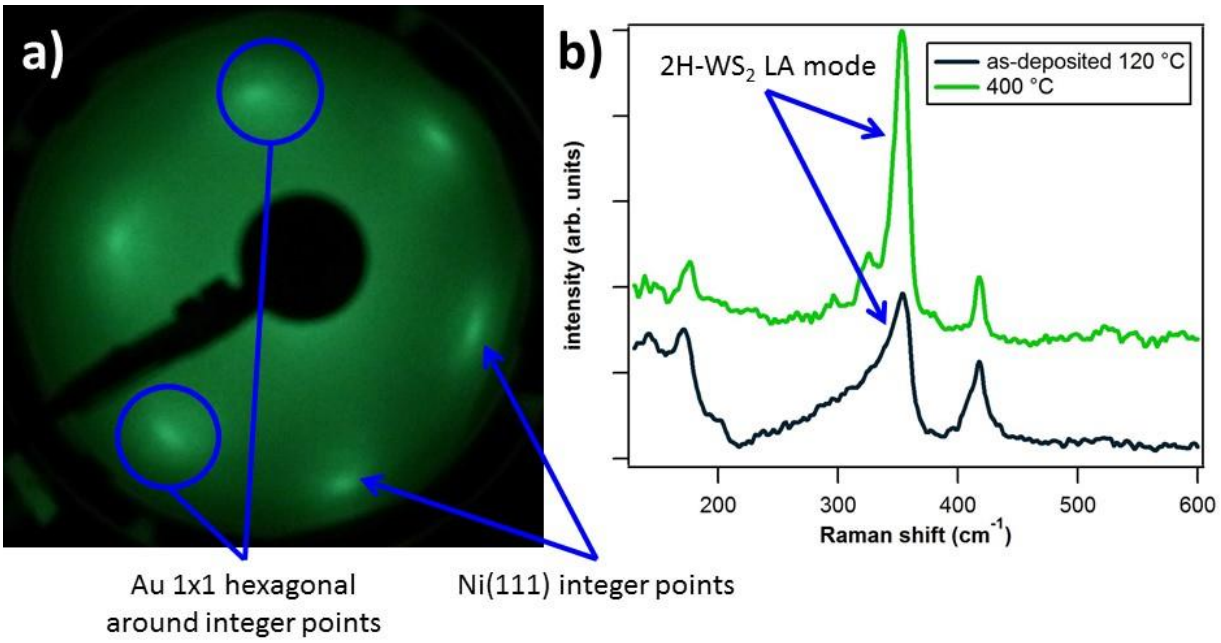

Figure 4.2.6 a) LEED image acquired at 60 eV for WS_2/Au/Ni(111) deposited at 400°C **b)** Raman spectra of WS_2/Au/Ni(111) acquired with a 532 nm laser before and after annealing

4.3 WS_2/h-BN/Ni(111)

Next, WS_2 was deposited on h-BN/Ni(111) system where the h-BN was grown via CVD using an ammonia borane complex (NH_3BH_3) at 10^{-6} mBar for 10 minutes. Because h-BN has a high affinity to the Ni(111) surface, the growth was considered self limiting and allowed to last for 10 minutes to ensure complete coverage. WS_2 was then grown by the method described earlier.

The XPS survey at PE50 revealed low content of B and N; however, this is likely due to the very low sensitivity of these two elements. Also, the W content is lower than a complete monolayer of coverage while the S demonstrated a similarly small peak as shown in Figure 4.3.1c. Initial deposition at 400°C yielded a highly convoluted W 4f peak, shown in Figure 4.3.1a, that exhibited no splitting. This is likely a result of a fast W deposition (5 minutes due to increased deposition efficiency), which may not have kinetically allowed enough time for the formation of an ordered phase.

The sample was then annealed at 400°C in a S atmosphere (10^{-8} mBar) for 15 minutes. After annealing, clear splitting between the W 4f 7/2 and 5/2 peaks developed where the peaks were respectively located at 32.3 eV and 34.3 eV; however, these peak positions are not exact due to fast scan times. Importantly, the S content of the system was doubled as demonstrated in Figure 4.3.1d. Because the as deposited sample exhibits sulfur deficiency as compared to other systems (see other sections) and the annealed sample, it is also possible that the as deposited sample is disordered, highly defective W metal. As a result of the fast W deposition, it is likely that the S in the chamber did not have time to migrate to the W surface and react to form WS_2. Instead, it is likely that the phase formed is primary metallic tungsten, evident by the large W 5p tail, with a mixture of various W and S containing species. Interestingly, annealing in S atmosphere generated the desired phase transition suggesting that the rate-limiting step may be mass transport of S to W deposited on the surface or the reaction between the two.

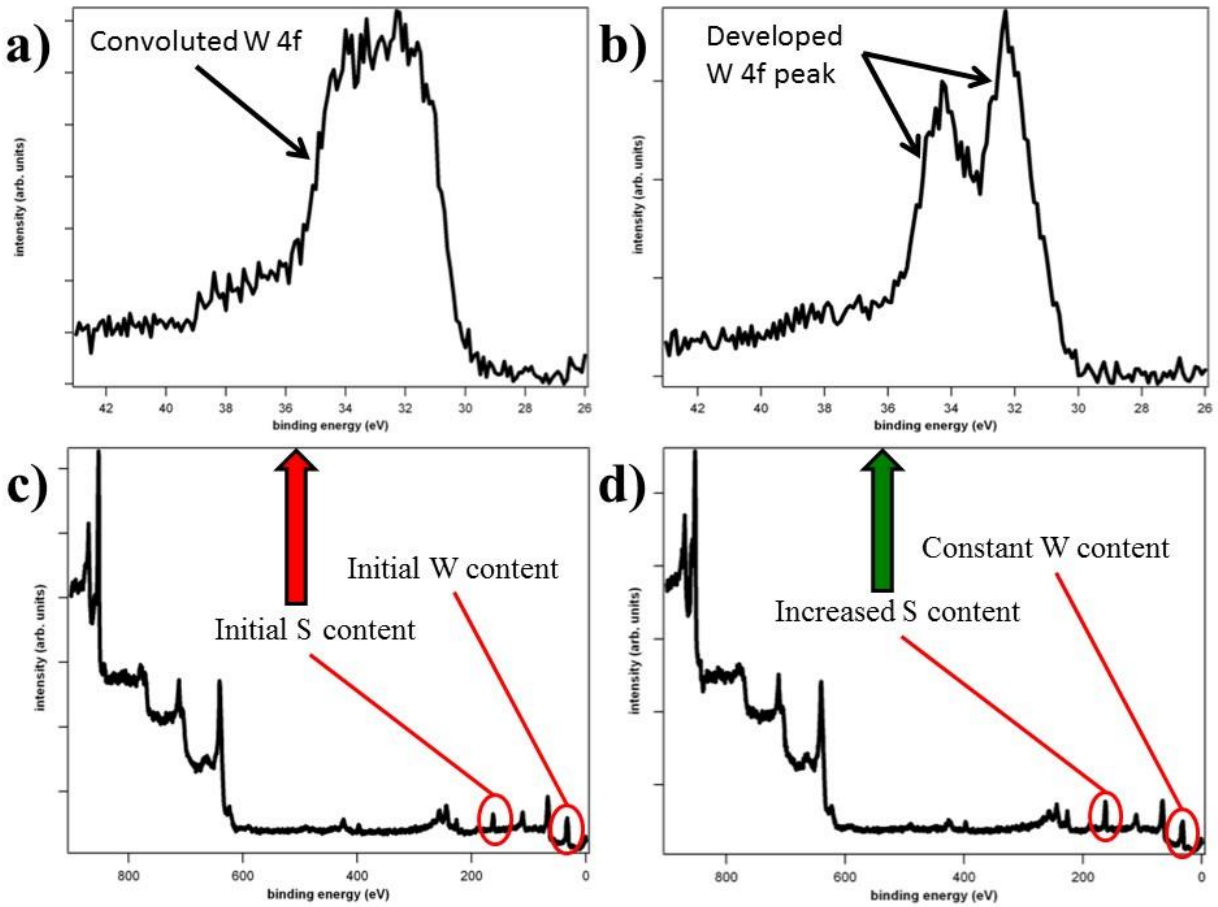

Figure 4.3.1 XPS spectra of WS_2/h-BN/Ni(111) **a)** of W 4f peaks as initially deposited at 400°C **b)** after annealing at 400°C for 15 minutes in a S background where peak splitting initiates **c)** survey spectra of the as deposited sample with very low S content **d)** XPS survey demonstrating increased S content after 400°C anneal in S background

This sample was then verified via Raman spectroscopy and found to be 2H-WS_2 by the existence of the resonant LA mode at 354 cm^{-1}. Because this sample was used for Raman spectroscopy and due to limited time, no UPS spectrum was measured for this sample. Despite not fully characterizing this system, important information can still be derived from it. Specifically, formation of WS_2 under UHV appears to be limited by the reaction with S. It is impossible to determine if the limiting factor is the reaction or mass transfer to the surface. Though the chamber is full of S, because the pressure is only ~10^{-8} mBar, it is difficult to determine how the process is limited.

4.4 WS_2/h-BN/Au/Ni(111)

The final system fabricated was WS_2/h-BN/Au/Ni(111) where h-BN was first deposited via methods described earlier on the clean Ni(111) surface. To reach a quasi-free standing state, Au was then deposited by thermal evaporation while annealing the crystal at 400°C. The Au intercalates underneath the h-BN and decouples it from the Ni(111) surface. Finally, WS_2 was deposited at 120°C by e-beam evaporating the W in a S atmosphere of 10^{-8} mBar.

The XPS survey, illustrated in **Figure 4.4.1**, reveals a low content of B, N, and W. The low content of B and N can be explained due to low sensitivity and decreased signal due attenuation from the WS_2 over layer. The decreased W content, ~0.5 ML, could be explained by low adherence to the h-BN surface while the S content remaining constant is likely due to S adsorption on exposed areas of transition metal.

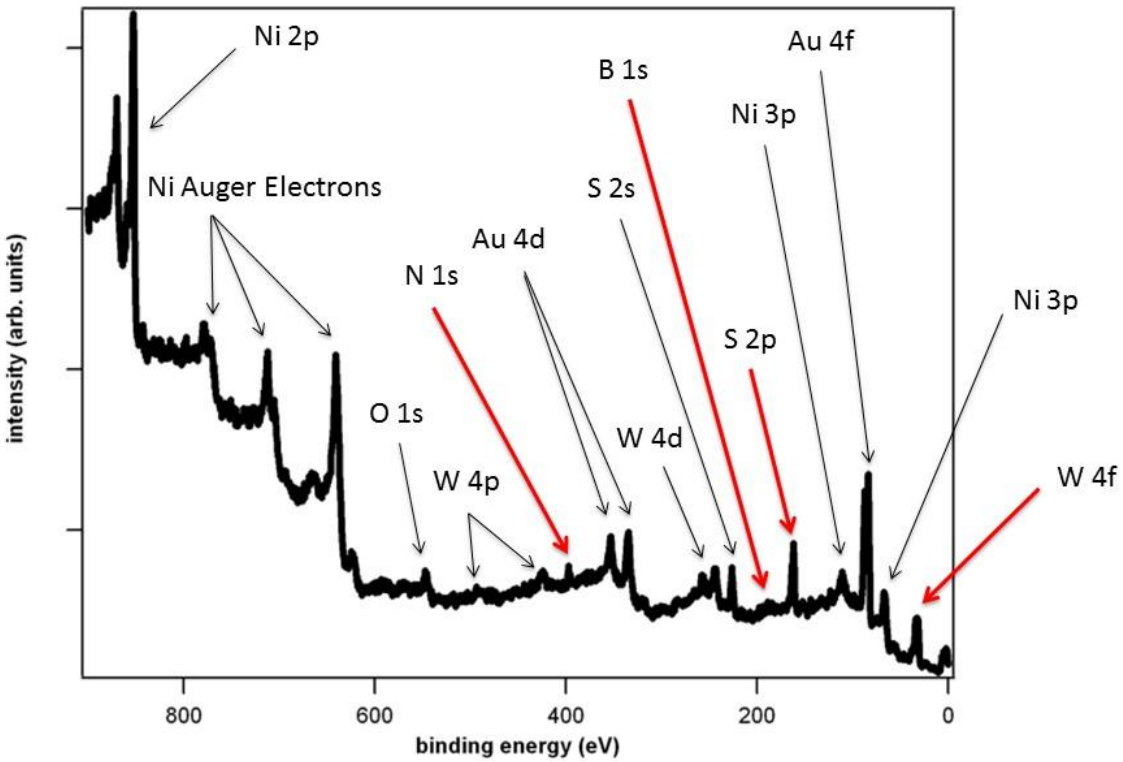

Figure 4.4.1 XPS survey at PE50 where a low signal is observed from B, N, and W; S content is consistent with 1 ML coverage while W is ~0.5 ML coverage

This sample was then annealed at 200°C, 300°C, and 400°C for 30 minutes and observed by XPS and UPS after each anneal. Again, with annealing, the W 4f peaks shift to higher binding energy. It is important to note that the S 2p peak does not exhibit a similar shift. In this case, both W 4f peaks, as deposited, are found at a higher binding energy than previously: 32.0 eV and 34.0 eV respectively. This shift may be a result of the reduced coupling between the WS_2/h-BN as compared to the WS_2/Au. Final peak positions for the W 4f 7/2 and 5/2 peaks are 32.3 eV and 34.3 eV thus maintaining their 2 eV separation.

Considering the Shirley background and fitting the 1T, 2H, WS3, and W 5p peaks, it is interesting to note a slight increase in 2H composition with annealing. The WS_3 content was found to decrease with annealing. The fits can be found below in **Figure 4.4.2** where the W 4f peak positions were shifted 0.1 eV to higher BE while maintaining constant separation. This trend is consistent with the trend found for the WS_2/Au/Ni(111) system but is much less profound. The less dramatic phase transition may be a result of phase stabilization on h-BN or the existence of small domain sizes; this is supported by the increased WS_3 content due to edge termination on S bonds and the likely formation of additional species at these edges. Thus, increased WS_3 suggests more edges and, consequently, smaller domains.

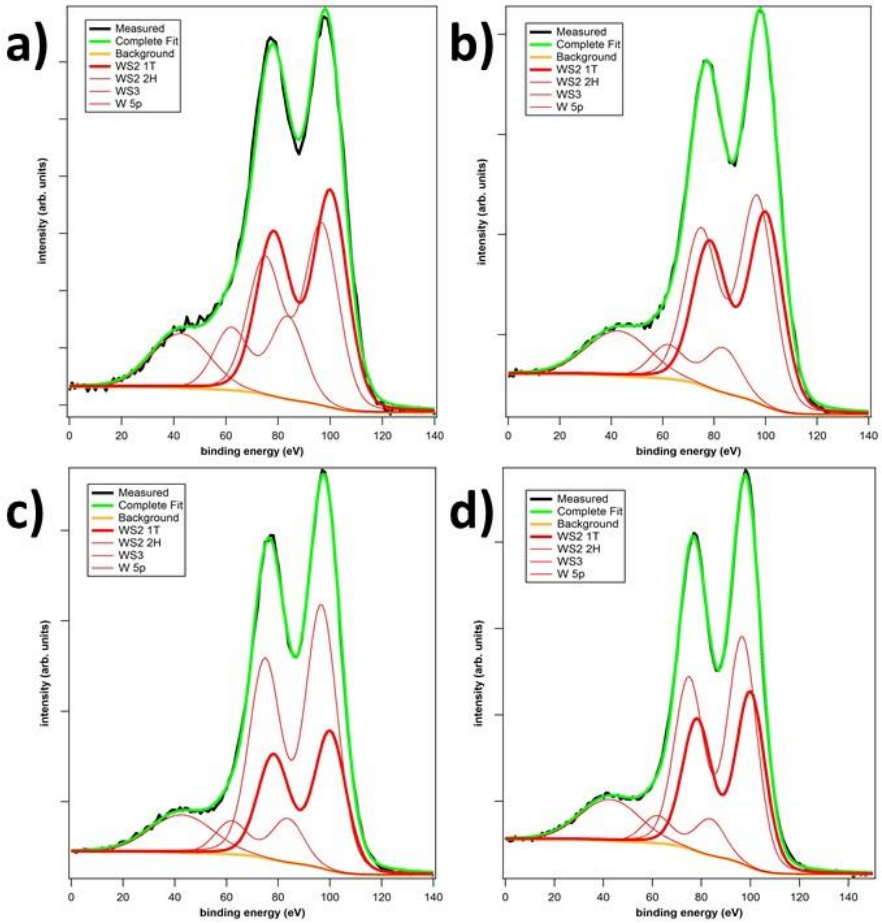

Figure 4.4.2 Fitted W 4f peaks for WS_2/h-BN/Au/Ni(111) considering 1T, 2H, WS_3, and W 5p peaks for **a)** as deposited at 120°C **b)** annealed at 200°C **c)** annealed at 300°C and **d)** annealed at 400°C; it is important to note the minimal change of 1T to 2H transformation that occurs with annealing compared to the dramatic transformation shown before for WS_2/Au/Ni(111)

UPS demonstrated a similar trend to before where increased annealing results in the development and growth of the σ-band of 2H-WS_2. UPS demonstrates visible band development for annealing as low as 200°C. Additional bands are observed in the valence band which can be attributed to the h-BN σ and π bands located further from the Fermi edge than the WS_2 bands. Again, defined states due to W and S orbital mixing can be observed in the spectrum shown in **Figure 4.4.3**. Interestingly, a small Γ_2^- state can be observed at annealing as low as 200°C. For the as deposited sample, Raman spectroscopy suggests highly reduced 2H content; this could be

a result of catalytic activity from the transition metal surface in the Au system or the reduced coupling between W/h-BN as compared to W/Au.

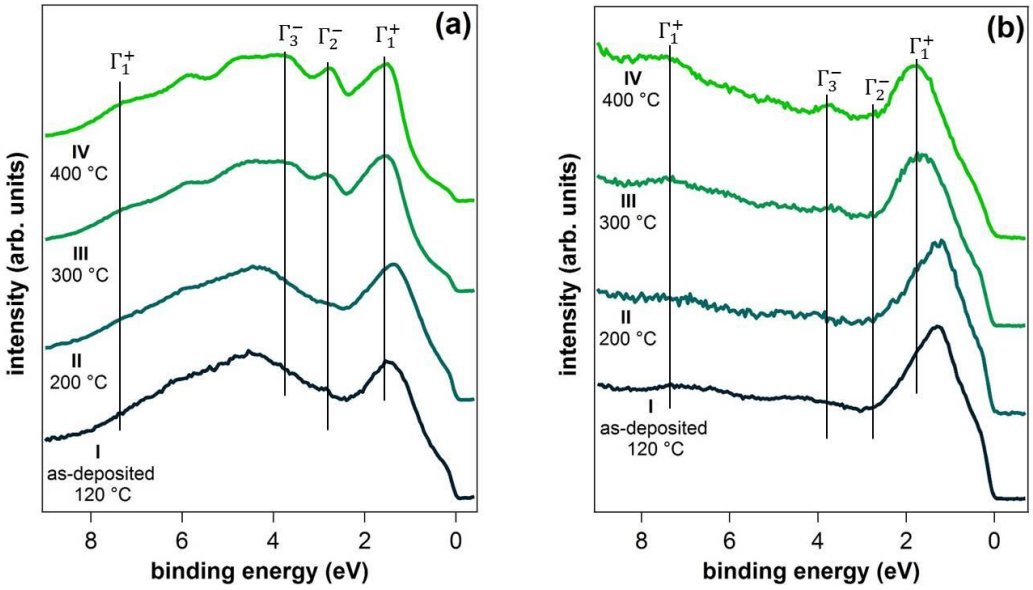

Figure 4.4.3 UPS spectra acquired with **a)** He-I PE 2 eV of WS_2/h-BN/Au/Ni(111) **I)** as deposited at 120°C and subsequently annealed at **II)** 200°C **III)** 300°C and **IV)** 400°C. The features are linked to the symmetry of the S p orbitals

Table 4.4.1 Calculated values for composition of 1T, 2H, and WS_3 as determined by the integrated intensities for W 4f peaks

Annealing temperature (°C)	Area components				Total Area	Fractional area				2H/(1T+2H)* 100
	1T	2H	WS3	5p		1T	2H	WS3	5p	
120	5827.39	4897.8	2226.98	1307	14259.2	40.8676	34.3484	15.6179	9.16603	45.6663
200	11958	12768	2773	2742	30241	39.5423	42.2208	9.16967	9.06716	51.638
300	8939	16896	2821	2542	31198	28.6525	54.1573	9.04225	8.14796	65.3997
400	11424	14788	2374	2898	28586	39.9636	51.7316	8.30476	10.1378	56.4169

Raman spectroscopy was measured on this sample before annealing (on the as deposited sample) and found a broad peak located convoluted on the edge of a metallic fluorescence peak.

As a result, it was concluded that the observed metallic phase is not 1T-WS_2 but is instead an amorphous WS_2 structure; this idea is supported by the lack of LEED pattern for WS_2 deposited below 400°C on any substrate. However, due to the valence band structure, it is believed that this structure is still metallic in character. Raman spectra and the LEED pattern can be found in **Figure 4.4.4**; while 2H content is visible in the as deposited sample, it is reduced when compared to the as deposited WS_2/Au system. Additionally, the LEED of annealed 2H-WS_2 is of low quality likely due to small domain sizes and low coverage.

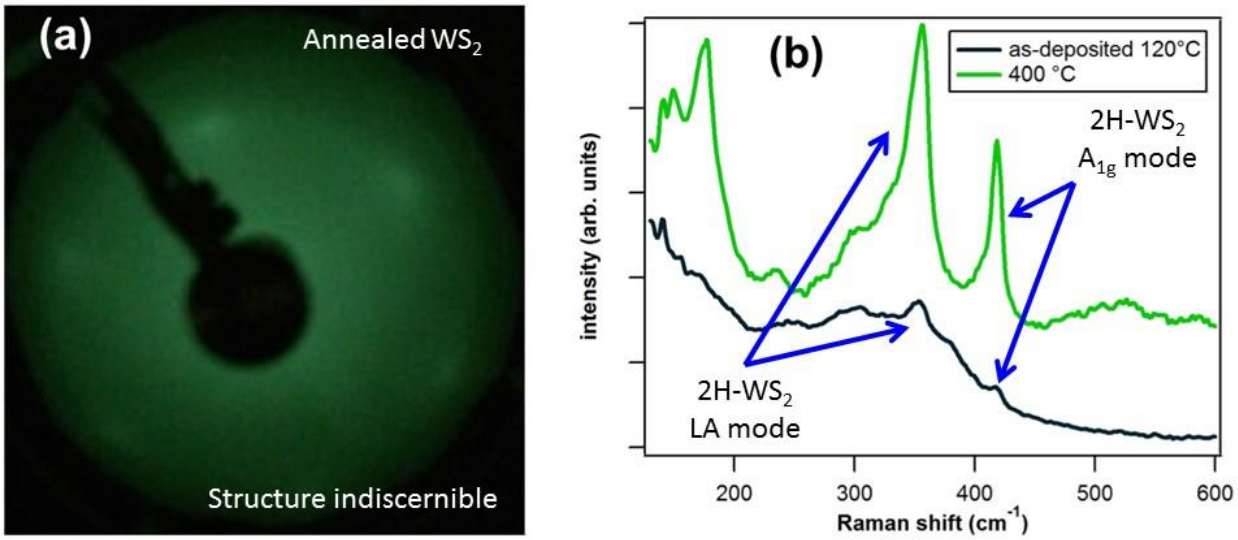

Figure 4.4.4 a) LEED acquired at 60 eV of WS_2/h-BN/Au/Ni(111) after annealing **b)** Raman spectroscopy WS_2/h-BN/Au/Ni(111) acquired with a 532 nm laser as deposited at 120°C and after annealing at 400°C

Despite the suggested amorphous structure, it is still feasibly possible to use this metallic WS_2 as very low resistance contacts to 2H-WS_2 for future microelectronic and optoelectronic applications. Raman spectroscopy for WS_2 on Au/Ni(111) and h-BN/Au/Ni(111) can be found in figure X, where clear artifacts relating to the 2H-WS_2 can be observed in both. Despite the presence of some 2H phase, valence band analysis suggests metallic character. The structure is likely primarily amorphous as suggested by the broad Raman features and lack of LEED. It is possible that nanocrystalline 2H-WS_2 is present in small amounts and acts as growth seeds

during subsequent annealing. Because the initial, low 2H presence, it is likely that a threshold percent composition is necessary for the semiconducting phase to become dominate.

5 Conclusions

This thesis has demonstrated the growth of h-BN on Cu foil, Pt(110) single crystal, and Ni(111) single crystal. It has also demonstrated the direct growth of a disordered, metallic WS_2 phase that can be irreversibly converted to semiconducting WS_2 upon annealing at $T \geq 300℃$ on multiple substrates including Ni(111) single crystal, amorphous Au, metallically coupled h-BN and quasi-free standing h-BN. The effects of growth parameters on film quality and electronic properties were investigated. Despite many interesting results presented in this thesis, many questions remain; for example, the crystallographic structure of the metallic phase along with the seed crystal size. More research is needed to better understand the growth mechanism for WS_2 on quasi-free standing h-BN in order to further improve the growth procedure. Future work may include further improving growth processes in order to achieve larger domains or continuous films in order to make electrical measurements. This chapter aims to summarize the major findings of this thesis and note where additional research is necessary.

5.1 Hexagonal Boron Nitride Growth

CVD Growth of h-BN on Cu foil was investigated in chapter 3 and it was found that substrate, gas flow over the substrate, and gas chemistry have a profound effect on growth. Raman spectroscopy used during initial growth identified the presence of defective BN compounds while SEM was used to observe monolayer domains. It was also found that ratio of AB:N_2 is important for growth where lower N_2 concentration allows for greater AB concentration at the surface and thus increased growth. Using an encapsulate to reduce the flow

rate of gas over the substrate also greatly improved growth while the use of electro-polished substrates enabled larger domains and reduced nucleation density.

The electronic structure of h-BN grown on Pt(110) was also investigated. Due to the low temperature of growth (630°C-730°C) low quality, low coverage h-BN was achieved; however, the coverage was high enough to make ARPES measurements. Band dispersions measured along the $\Gamma - K$ direction indicated low quality h-BN due to band smearing from defects. Additional experiments involving h-BN, outlined in chapter 4.3 and 4.4, included direct growths of different phases of WS_2 grown in UHV and demonstrate the feasibility using h-BN as a dielectric substrate for 2D semiconducting devices.

5.2 Tungsten Disulfide Growth

Direct growth and *in-situ* characterization of metallic and semiconducting WS_2 on various substrates was investigated in chapter 4. It was found that a disordered, metallic phase can be grown at 120°C and irreversibly transformed into the thermodynamically stable, semiconducting phase with annealing at T > 300°C. This effect was observed on Au/Ni(111), h-BN/Ni(111), and h-BN/Au/Ni(111). The change was characterized by XPS shifting of the W 4f peaks to higher BE characteristic of 2H-WS_2. The metallic phase is disordered despite the XPS emission characteristic of 1T-WS_2 and suggests that previous studies may inaccurately attributed this signal to 1T-WS_2. While no LEED pattern was discernable for the metallic phase, LEED patterns consistent with 2H-WS_2 were observed after annealing. Finally, the phase transformation was best observed in valence band measurements where a band ~1.7 eV from the conduction band, not present in the disordered phase, evolved with annealing.

Raman spectroscopy verified the presence of 2H-WS_2 after annealing and identified the presence of limited 2H nature in the disordered sample. It is likely that small 2H domains were

able to form during low temperature growth while the majority of the deposited area was disordered. As the samples were annealed, the atoms on the surface were able to move more freely and reorder thus transforming into the thermodynamically stable 2H phase. WS_2 deposited at low temperature on Au demonstrated a larger fraction of 2H as compared to the disordered phase than WS_2 deposited on quasi-free standing h-BN. This can be attributed to coupling between the TMD and the transition metal surface where transition metal surfaces often behave catalytically.

These results demonstrate the feasibility of directly growing metallic WS_2 for ultra low resistance contacts to WS_2 devices thus making 2D devices more viable. It also suggest an alternative explanation to previous works that attribute lower BE XPS emission lines to 1T-WS_2 and attributes this phenomena to a disordered phase that maintains the metallic nature of the 1T phase.

6 References

(1) Butler, S. Z.; Hollen, S. M.; Cao, L.; Cui, Y.; Gupta, J. a.; Gutiérrez, H. R.; Heinz, T. F.; Hong, S. S.; Huang, J.; Ismach, A. F.; Johnston-Halperin, E.; Kuno, M.; Plashnitsa, V. V.; Robinson, R. D.; Ruoff, R. S.; Salahuddin, S.; Shan, J.; Shi, L.; Spencer, M. G.; Terrones, M.; Windl, W.; Goldberger, J. E. *ACS Nano* **2013**, *7*, 2898–2926.

(2) May, J. W. *Surf. Sci.* **1969**, *17*, 267–270.

(3) Novoselov, K. S.; Geim, a K.; Morozov, S. V; Jiang, D.; Zhang, Y.; Dubonos, S. V; Grigorieva, I. V; Firsov, a a. *Science* **2004**, *306*, 666–669.

(4) Bednorz, J. G.; Miiller, K. A. *Condens. Matter* **1986**, *193*, 189–193.

(5) Kamihara, Y.; Watanabe, T.; Hirano, M.; Hosono, H. *Communications* **2008**, 3296–3297.

(6) Frindt, R. F. *J. Appl. Phys.* **1966**, *37*, 1928–1929.

(7) Bresnehan, M. S. Synthesis and Characterization of Hexagonal Boron Nitride for Integration with Graphene Electronics, The Pennsylvania State University, 2013, p. 224.

(8) Arya, S. P. S.; Elettrica, I.; Aquila, U. L. *Thin Solid Films* **1988**, *157*, 267–282.

(9) Kurdyumov, a. V.; Solozhenko, V. L.; Zelyavski, W. B. *J. Appl. Crystallogr.* **1995**, *28*, 540–545.

(10) Nagashima, a.; Tejima, N.; Gamou, Y.; Kawai, T.; Oshima, C. *Phys. Rev. Lett.* **1995**, *75*, 3918–3921.

(11) Kobayashi, Y.; Akasaka, T.; Makimoto, T. *J. Cryst. Growth* **2008**, *310*, 5048–5052.

(12) Schmolla, W.; Hartnagel, H. L. *Solid. State. Electron.* **1983**, *26*, 931–939.

(13) Hirayama, M. *J. Electrochem. Soc.* **1975**, *122*, 1671.

(14) Yamaguchi, E.; Minakata, M. *J. Appl. Phys.* **1984**, *55*, 3098–3102.

(15) Pedersen, H.; Chubarov, M.; Högberg, H.; Jensen, J.; Henry, A. *Thin Solid Films* **2012**, *520*, 5889–5893.

(16) Gómez-Aleixandre, C.; Essafti, a.; Fernández, M.; Fierro, J. L. G.; Albella, J. M. *J. Phys. Chem.* **1996**, *100*, 2148–2153.

(17) Mantovan, R.; Georgieva, M. *Acta Phys. …* **2007**, *112*, 1271–1280.

(18) Rand, M. J.; Roberts, J. F. *J. Electrochem. Soc.* **1968**, *115*, 423.

(19) Sichel, E. K.; Miller, R. E.; Abrahams, M. S.; Buiocchi, C. J. *Phys. Rev. B* **1976**, *13*, 4607–4611.

(20) Solozhenko, V. L.; Turkevich, V. Z.; Holzapfel, W. B. *J. Phys. Chem. B* **1999**, *103*, 2903–2905.

(21) Kern, G.; Kresse, G.; Hafner, J. *Phys. Rev. B* **1999**, *59*, 8551–8559.

(22) Wang, Q. H.; Kalantar-Zadeh, K.; Kis, A.; Coleman, J. N.; Strano, M. S. *Nat. Nanotechnol.* **2012**, *7*, 699–712.

(23) Berkdemir, A.; Gutiérrez, H. R.; Botello-Méndez, A. R.; Perea-López, N.; Elías, A. L.; Chia, C.-I.; Wang, B.; Crespi, V. H.; López-Urías, F.; Charlier, J.-C.; Terrones, H.; Terrones, M. *Sci. Rep.* **2013**, *3*, 1755.

(24) Ghorbani-Asl, M.; Borini, S.; Kuc, a.; Heine, T. *Phys. Rev. B - Condens. Matter Mater. Phys.* **2013**, *87*, 1–6.

(25) Kaul, A. B. *J. Mater. Res.* **2014**, *29*, 348–361.

(26) Chhowalla, M.; Shin, H. S.; Eda, G.; Li, L.-J.; Loh, K. P.; Zhang, H. *Nat. Chem.* **2013**, *5*, 263–275.

(27) Mak, K. F.; Lee, C.; Hone, J.; Shan, J.; Heinz, T. F. *Phys. Rev. Lett.* **2010**, *105*, 2–5.

(28) Chianelli, R. R.; Siadati, M. H.; De la Rosa, M. P.; Berhault, G.; Wilcoxon, J. P.; Bearden, R.; Abrams, B. L. *Catal. Rev.* **2006**, *48*, 1–41.

(29) Mahler, B.; Hoepfner, V.; Liao, K.; Ozin, G. *J. Am. Chem. Soc.* **2014**, *136*, 14121–14127.

(30) Ding, Y.; Wang, Y.; Ni, J.; Shi, L.; Shi, S.; Tang, W. *Phys. B Condens. Matter* **2011**, *406*, 2254–2260.

(31) Zeng, Z.; Yin, Z.; Huang, X.; Li, H.; He, Q.; Lu, G.; Boey, F.; Zhang, H. *Angew. Chemie - Int. Ed.* **2011**, *50*, 11093–11097.

(32) Ma, Y.; Dai, Y.; Guo, M.; Niu, C.; Lu, J.; Huang, B. *Phys. Chem. Chem. Phys.* **2011**, *13*, 15546–15553.

(33) Lin, Y.-C.; Dumcenco, D. O.; Huang, Y.-S.; Suenaga, K. *Nat. Nanotechnol.* **2014**, *9*, 391–396.

(34) Zhou, B.; Yang, L. X.; Chen, F.; Xu, M.; Wu, T.; Wu, G.; Chen, X. H.; Feng, D. L. *J. Phys. Chem. Solids* **2011**, *72*, 474–478.

(35) Zabinski, J. S.; Donley, M. S.; Prasad, S. V.; McDevitt, N. T. *J. Mater. Sci.* **1994**, *29*, 4834–4839.

(36) Kuc, a.; Zibouche, N.; Heine, T. *Phys. Rev. B* **2011**, *83*, 1–4.

(37) Fang, H.; Battaglia, C.; Carraro, C.; Nemsak, S.; Ozdol, B.; Kang, J. S.; Bechtel, H. a; Desai, S. B.; Kronast, F.; Unal, A. a; Conti, G.; Conlon, C.; Palsson, G. K.; Martin, M. C.; Minor, A. M.; Fadley, C. S.; Yablonovitch, E.; Maboudian, R.; Javey, A. *Proc. Natl. Acad. Sci. U. S. A.* **2014**, *111*, 6198–6202.

(38) Yang, J.; Voiry, D.; Ahn, S. J.; Kang, D.; Kim, A. Y.; Chhowalla, M.; Shin, H. S. *Angew. Chemie - Int. Ed.* **2013**, *52*, 13751–13754.

(39) Jaramillo, T. F.; Jørgensen, K. P.; Bonde, J.; Nielsen, J. H.; Horch, S.; Chorkendorff, I. *Science* **2007**, *317*, 100–102.

(40) Pettenkofer, J. C. *Physics (College. Park. Md).* **1989**, *35*, 439–442.

(41) Enyashin, A. N.; Yadgarov, L.; Houben, L.; Popov, I.; Weidenbach, M.; Tenne, R.; Bar-Sadan, M.; Seifert, G. *J. Phys. Chem. C* **2011**, *115*, 24586–24591.

(42) Bryant, W. *J. Mater. Sci.* **1977**, *12*, 1285–1306.

(43) Jasinski, J. M.; Meyerson, B. S.; Scott, B. A. *Ann. Rev. Phys. Chem.* **1987**, *38*, 109–140.

(44) Choy, K. *Prog. Mater. Sci.* **2003**, *48*, 57–170.

(45) Tang, Q.; Zhou, Z. *Prog. Mater. Sci.* **2013**, *58*, 1244–1315.

(46) Kern, W.; Schnable, G. *IEEE* **1979**, *26*, 647–657.

(47) Campbell, S. A. (University of M. *Fabrication Engineering at the Micro and Nanoscale*; 2008; p. 637.

(48) Nagel, S. R.; Walker, K. L. **1982**.

(49) Niu, T.; Li, A. *Prog. Surf. Sci.* **2015**, *90*, 21–45.

(50) Hersee, S. D.; Duchemin, J. P. *Ann. Rev. Mater. Sci.* **1982**, *12*, 65–80.

(51) Eichfeld, S. M.; Hossain, L.; Lin, Y.; Piasecki, A. F.; Kupp, B.; Birdwell, A. G.; Burke, R. A.; Lu, N.; Peng, X.; Li, J.; Azcatl, A.; Mcdonnell, S.; Wallace, R. M.; Kim, M. J.; Mayer, T. S.; Redwing, J. M.; Robinson, J. A. **2015**, 2080–2087.

(52) Reichelt, K.; Jiang, X. *Thin Solid Films* **1990**, *191*, 91–126.

(53) Helmersson, U.; Lattemann, M.; Bohlmark, J.; Ehiasarian, A. P.; Gudmundsson, J. T. *Thin Solid Films* **2006**, *513*, 1–24.

(54) Shen, Z.-X. **2003**, 22.

(55) Hertz, H. *Ann. Phys.* **1887**, *31*, 983.

(56) Einstein, A. *Ann. Phys.* **1906**, *325*, 199.

(57) Rotenberg, E. *The Bandstructure of Solids by Angle-Resolved Photoemission: A brief introduction to solid state physics*; 1996.

(58) Dessau, D. *Angle Resolved Photoemission Spectroscopy*; 2004; pp. 1–55.

(59) Damascelli, A. *State-of-the-Art ARPES: Momentum-Space Microscopy of Sr2RuO4 and Bi2212*.

(60) Osada, M.; Sasaki, T. *Adv. Mater.* **2012**, *24*, 210–228.

(61) Gorbachev, R. V.; Riaz, I.; Nair, R. R.; Jalil, R.; Britnell, L.; Belle, B. D.; Hill, E. W.; Novoselov, K. S.; Watanabe, K.; Taniguchi, T.; Geim, A. K.; Blake, P. *Small* **2011**, *7*, 465–468.

Academic Vita

Brian D. Markman
brian.markman8@gmail.com
1664 Aidenn Lair Rd.
Dresher, PA 19025
(215)-264-9890

Education

The Pennsylvania State University
Schreyer Honors College
B.S. in Materials Science and Engineering
Minor in Electronic and Photonic Materials
Dean's List: Fall 2011-Spring 2015

Work Experience

1. ARPES Investigation of 2D Materials on Various Substrates
   Fall 2014
   International Visiting Undergraduate Researcher
   Universitá degli studi Padova, Padova, Italy
2. National Nanotechnology Infrastructure Network REU
   Summer 2014
   Undergraduate Researcher
   University of California Santa Barbara, Santa Barbara, CA
3. Surface and Thin Film REU
   Summer 2013
   Undergraduate Researcher
   University of Virginia, Charlottesville, VA

Publications

- H. Qian, B. D. Markman, and N. C. Giebink, “Vector vortex beam emission from organic semiconductor microlasers” *Appl. Phys Lett. 103, 161110 (2013)*
- B. D. Markman, R. R. Ranade and N. C. Giebink, "Nonimaging optics in luminescent solar concentration" *Opt. Express 20, A622 (2012)*

Leadership

- Assistant Captain of 2 National Championship ice hockey teams (2008 and 2010)
- Lead Instructor and Course Manager of Twining Valley Golf Club 2009 – 2013